

JOINT MIGRATION VELOCITY ANALYSIS OF PP- AND
PS-WAVES FOR VTI MEDIA

by
Pengfei Cai

© Copyright by Pengfei Cai, 2013

All Rights Reserved

A thesis submitted to the Faculty and the Board of Trustees of the Colorado School of Mines in partial fulfillment of the requirements for the degree of Master of Science (Geophysics).

Golden, Colorado

Date _____

Signed: _____
Pengfei Cai

Signed: _____
Prof. Ilya Tsvankin
Thesis Advisor

Golden, Colorado

Date _____

Signed: _____
Terry Young
Professor and Head
Department of Geophysics

ABSTRACT

Combining PP-waves with mode-converted PS reflections in migration velocity analysis (MVA) can help build more accurate VTI (transversely isotropic with a vertical symmetry axis) velocity models. To avoid problems caused by the moveout asymmetry of PS-waves and take advantage of efficient MVA algorithms designed for pure modes, I suggest to generate pure SS-reflections from PP and PS data using the PP+PS=SS method. Then the residual moveout in both PP and SS common-image gathers is minimized during iterative velocity updates. The model is divided into square cells, and the VTI parameters V_{P0} , V_{S0} , ϵ , and δ are defined at each grid point. The objective function also includes the differences between the migrated depths of the same reflectors on the PP and SS sections and a regularization term. Synthetic examples confirm that 2D MVA of PP- and PS-waves may be able to resolve all four relevant parameters of VTI media if reflectors with at least two distinct dips are available. The algorithm is also applied to a 2D line from 3D OBS (ocean bottom seismic) data acquired at Volve field in the North Sea. After the anisotropic velocity model has been reconstructed, accurate depth images can be obtained by migrating the recorded PP and PS data.

TABLE OF CONTENTS

ABSTRACT	iii
LIST OF FIGURES	v
LIST OF TABLES	viii
ACKNOWLEDGMENTS	ix
CHAPTER 1 INTRODUCTION	1
CHAPTER 2 IMPLEMENTATION OF THE PP+PS=SS METHOD	5
CHAPTER 3 2D JOINT MIGRATION VELOCITY ANALYSIS FOR VTI MEDIA	12
CHAPTER 4 SYNTHETIC TESTS	19
4.1 Models composed of homogeneous layers	19
4.2 Model with heterogeneous layers	26
CHAPTER 5 APPLICATION TO FIELD DATA	42
CHAPTER 6 CONCLUSIONS AND RECOMMENDATIONS	52
6.1 Recommendations for future work	53
REFERENCES CITED	55
APPENDIX - PARAMETER-UPDATING METHODOLOGY	58

LIST OF FIGURES

2.1	PP traveltimes recorded in a common-receiver gather (after Grechka and Tsvankin, 2002).	7
2.2	Matching the horizontal slownesses on common-receiver PP and PS sections at locations x_1 and x_2 helps find the source-receiver coordinates x_3 and x_4 of the pure SS ray x_3Rx_4 . This reconstructed SS ray has the same reflection point R as the PP ray x_1Rx_2 and PS rays x_1Rx_3 and x_2Rx_4 (after Grechka and Tsvankin, 2002).	8
2.3	Critical (maximum) offset of the constructed SS-waves in a horizontal layer (Tsvankin & Grechka, 2011).	9
2.4	Constructed CMP gathers of SS-waves before interpolation.	10
2.5	Gathers from Figure 2.4 after interpolation.	11
3.1	Gridded model for reflection tomography.	14
3.2	(a) PP-wave moveout and (b) SS-wave moveout.	15
3.3	Reflection points may be imaged at different depths on PP and SS sections.	16
4.1	Model with a VTI layer embedded between two isotropic layers. The P- and S-wave velocities in the top layer are $V_P = 2000$ m/s and $V_S = 1000$ m/s; for the second layer, $V_{P0} = 3000$ m/s, $V_{S0} = 1500$ m/s, $\epsilon = 0.1$, and $\delta = -0.1$	20
4.2	Common-image gathers of (a) PP-waves and (b) SS-waves (displayed every 100 m) after migration with the initial model.	21
4.3	(a) PP-wave and (b) SS-wave depth images computed with the initial model.	22
4.4	CIGs of (a) PP-waves and (b) SS-waves after migration with the inverted model.	22
4.5	Final depth images of (a) PP-waves and (b) SS-waves with the inverted parameters for the model in Figure 4.1.	23

4.6	Three-layer model with dipping interfaces. The parameters of the first isotropic layer are $V_P = 2000$ m/s, $V_S = 1000$ m/s; for the second VTI layer, $V_{P0} = 3000$ m/s, $V_{S0} = 1500$ m/s, $\epsilon = 0.2$, and $\delta = 0.1$. The maximum dip of both reflectors is 27°	24
4.7	CMP gathers of the recorded (a) PP-waves and (b) PS-waves at location 3000 m. (c) The SS data constructed by the PP+PS=SS method at the same location.	25
4.8	Common-image gathers of (a) PP-waves and (b) SS-waves (displayed every 100m) after migration with the initial model.	26
4.9	(a) PP-wave and (b) SS-wave depth images computed with the initial model.	27
4.10	CIGs of (a) PP-waves and (b) SS-waves after migration with the inverted model.	27
4.11	Final depth images of (a) PP-waves and (b) SS-waves obtained with the inverted parameters for the model in Figure 4.6.	28
4.12	Model with a factorized VTI layer embedded between two isotropic homogeneous layers. (a) The density, the vertical velocities (b) V_{P0} and (c) V_{S0} , and the anisotropy parameters (d) ϵ and (e) δ . The parameters of the top layer are $V_P = 2000$ m/s and $V_S = 1000$ m/s. For the second layer, the vertical velocities at the point marked by a black dot on the left are $V_{P0} = 1850$ m/s and $V_{S0} = 925$ m/s. Both V_{P0} and V_{S0} vary linearly with the lateral gradients $k_{p,x} = 0.05s^{-1}$ and $k_{s,x} = 0.025s^{-1}$ and vertical gradients $k_{p,z} = 0.4s^{-1}$ and $k_{s,z} = 0.2s^{-1}$ so that $V_{P0}/V_{S0} = 1/2$. The anisotropy parameters of the VTI layer are constant: $\epsilon = 0.1$ and $\delta = -0.1$	29
4.13	Common-image gathers of (a) PP-waves and (b) SS-waves (displayed every 100m) after migration with the initial model.	31
4.14	(a) PP-wave and (b) SS-wave depth images computed with the initial model.	32
4.15	CIGs of (a) PP-waves and (b) SS-waves after migration with the inverted model.	33
4.16	(a) PP-wave and (b) SS-wave depth images computed with the inverted parameters for the model in Figure 4.12.	34

4.17	Common-image gathers of (a) PP-waves and (b) SS-waves (displayed every 100m) after migration with the initial model. . . .	36
4.18	(a) PP-wave and (b) SS-wave depth images computed with the initial model parameters.	37
4.19	Velocities (a) V_{P0} and (b) V_{S0} for the model in Figure 4.12 estimated on a grid. Inverted layer-based parameters (c) ϵ and (d) δ	38
4.20	Common-image gathers of (a) PP-waves and (b) SS-waves (displayed every 100m) after migration with the estimated model. . .	39
4.21	(a) PP-wave and (b) SS-wave depth images computed with the estimated model parameters.	40
4.22	Depth mistie between the initial (a) PP-wave and (b) SS-wave images. The (c) PP-wave and (d) SS-wave images computed with the inverted model are tied in depth.	41
5.1	(a) Location of Volve field in the North Sea (figure courtesy of Statoil) and (b) a representative geologic cross-section of Volve field (after Akalin <i>et al.</i> , 2010).	43
5.2	Geometry of the Volve 3D OBS survey. A pair of cables (black lines) was put on the seafloor with 400 m separation, and shots were aquired in a 12 km \times 2.4 km rectangular area (gray). There was an 800 m moveup between swaths (after Wang, 2012).	44
5.3	Initial VTI model for line y=2.8 km. The vertical velocities (a) V_{P0} and (b) V_{S0} and the anisotropy parameters (c) ϵ and (d) δ	45
5.4	(a) PP- and (b) PS-wave images generated by Kirchhoff prestack depth migration with the initial model.	47
5.5	Image of the constructed SS-waves generated with the initial model.	48
5.6	Estimated VTI model for line y=2.8 km from the Volve survey. The vertical velocities (a) V_{P0} and (b) V_{S0} and the anisotropy parameters (c) ϵ and (d) δ	49
5.7	(a) PP- and (b) SS-wave depth images generated with the estimated model from Figure 5.6.	50
5.8	PS-wave depth image generated with the estimated model.	51

LIST OF TABLES

4.1	Inversion results for the VTI layer from the model in Figure 4.12. The velocities V_{P0} and V_{S0} are correctly assumed to vary linearly inside the layer, and ϵ and δ are spatially invariant.	30
-----	---	----

ACKNOWLEDGMENTS

I would like to acknowledge the support provided by the Consortium Project on Seismic Inverse Methods for Complex Structures at the Center for Wave Phenomena (CWP). This project would never have succeeded without the help of my thesis advisor Ilya Tsvankin and the other two committee members, Thomas L. Davis and Walt Lynn. Ilya's initial guidance helped me become familiar with the project. Whenever I encountered problems, he was always patient, and his understanding and suggestions always encouraged me to move on. Thomas' broad knowledge of multicomponent data analysis and Walt's expertise in seismic data processing also contributed a lot to my research.

Deep thanks go to Xiaoxiang Wang, whose research work has built the basis for my master's thesis. His publications and computer codes were valuable sources for my research. I am also grateful to John Stockwell who helped me learn to use Seismic Unix. His support with SU enabled me to progress quickly at the beginning of my research. Thanks to James Gaiser from Geokinetics for his helpful discussions. I also appreciate Diane Witters for her valuable advice on my writing. I want to thank the members of the A(nisotropy)-Team of the Center for Wave Phenomena for fruitful discussions. Thanks also go to my CWP colleagues for valuable technical assistance. My research also benefited from the field data obtained from Statoil with Paul Sava's help. I would like to thank Statoil ASA and the Volve license partners ExxonMobil E&P Norway and Bayerngas Norge for the release of the Volve dataset. The viewpoints about the Volve data in this thesis are of the author and do not necessarily reflect the views of Statoil ASA and the Volve field license partners.

Finally I thank my parents and my sister for keeping watch on my progress during the thesis work. The love from my family always warms me up and leads me forward.

CHAPTER 1

INTRODUCTION

Transversely isotropic (TI) models have been widely used in exploration seismology (Tsvankin, 2005). Seismic signatures in TI media depend only on the angle between the propagation direction and the symmetry axis. Any plane that contains the symmetry axis represents a plane of mirror symmetry; one more symmetry plane (the “isotropy plane”) is normal to the symmetry axis. Velocities in the isotropy plane do not change with direction because the angle between the propagation direction and the symmetry axis remains equal to 90° . TI media with a vertical symmetry axis (VTI) represent the most common anisotropic model in industry for depth imaging.

Prestack depth migration (PSDM) and reflection tomography in the migrated domain are common tools in P-wave imaging (Stork, 1992; Wang *et al.*, 1995; Adler *et al.*, 2008; Bakulin *et al.*, 2010). Most current PSDM and migration velocity analysis (MVA) algorithms account for transverse isotropy with a vertical (VTI) or tilted (TTI) symmetry axis. Sarkar & Tsvankin (2004) develop an efficient MVA method for VTI media by dividing the model into so called “factorized” blocks. Within each block, the anisotropy parameters are constant, while the P-wave symmetry-direction velocity V_{P0} varies linearly in space. To extend MVA to more complex subsurface structures, Wang & Tsvankin (2012) suggest a P-wave ray-based tomographic algorithm in which the parameters V_{P0} , ϵ , and δ are defined on a rectangular grid. Similar multiparameter tomographic inversion is applied to synthetic and field P-wave data by Zhou *et al.* (2011).

To resolve the velocity V_{P0} and anisotropy parameters ϵ and δ required for P-wave depth imaging, it is necessary to combine P-wave traveltimes with additional information. Tsvankin & Thomsen (1995) demonstrate that long-spread (nonhyperbolic)

P- and SV-wave moveouts are sufficient for estimating the VTI parameters V_{P0} , ϵ , δ , and the SV-wave vertical velocity V_{S0} . However, it is more practical to supplement P-waves with converted PS(PSV) data. For 2D VTI models, the parameters V_{P0} , V_{S0} , ϵ , and δ can be obtained by combining PP- and PS-wave traveltimes for a horizontal and dipping interface (Tsvankin & Grechka, 2000).

Multicomponent data can improve reservoir imaging and provide useful information for lithology, fluid, and fracture characterization. For example, shear waves help in imaging of reservoirs beneath gas clouds, where P-waves suffer from high attenuation (Tsvankin, 2005). For typical multicomponent surveys, geophones record both P-waves and mode-converted PS-waves. Compared to P-waves, PS-waves are usually more sensitive to anisotropy parameters and also provide information about shear-wave velocities. These advantages can help constrain model parameters when inversion of P-wave data is nonunique.

Several authors discuss joint tomographic inversion of PP and PS data (Stopin & Ehinger, 2001; Audebert *et al.*, 1999; Broto *et al.*, 2003; Foss *et al.*, 2005). However, velocity analysis of mode conversions is hampered by the asymmetry of PS moveout (i.e. PS traveltimes generally do not stay the same when the source and receiver are interchanged) and polarity reversals of PS-waves. As discussed by Thomsen (1999) and Tsvankin & Grechka (2011), the apex of the PS moveout in common-midpoint (CMP) gathers typically is shifted from zero offset. Therefore, MVA for PS-waves (Du *et al.*, 2012; Foss *et al.*, 2005; Audebert *et al.*, 1999) has to account for the “diodic” nature of PS reflections (Thomsen, 1999). For example, common-image gathers (CIGs) of PS-waves can be computed separately for positive and negative offsets in the tomographic objective function (Foss *et al.*, 2005).

To replace mode conversions in velocity analysis with pure SS reflections, Grechka & Tsvankin (2002b) suggest the so-called PP+PS=SS method. By combining PP and PS events that share P-legs, that method generates SS reflection data with the correct

kinematics. Grechka *et al.* (2002a) perform joint inversion of PP and PS reflection data using stacking-velocity tomography, which operates with NMO velocities for 2D lines and NMO ellipses for wide-azimuth 3D surveys (Grechka *et al.*, 2002b). They construct SS traveltimes with the PP+PS=SS method and then apply stacking-velocity tomography to the PP and SS data. However, their methodology is limited to hyperbolic moveout and excludes information contained in long-offset traveltimes (Tsvankin & Grechka, 2011). Also, stacking-velocity tomography can be applied only to relatively simple layered or blocked models.

To make use of the efficient MVA techniques developed for pure modes (Sarkar & Tsvankin, 2004; Wang & Tsvankin, 2012), here I apply the PP+PS=SS method to construct pure SS-wave reflections from PP and PS data. The MVA is performed by minimizing residual moveout of reflection events in both PP- and SS-wave CIGs. The velocity updating for P-wave data is based on the ray-based gridded tomography developed by Wang & Tsvankin (2012). PP and PS images of the same reflector do not match in depth if the velocity model is incorrect (Foss *et al.*, 2005; Tsvankin & Grechka, 2011). Therefore, in addition to flattening image gathers, I penalize depth misties between PP and PS sections.

Seismic reflection tomography is generally ill-posed, so a priori geologic information should be incorporated into the inversion problem to mitigate the nonuniqueness. For example, it is often assumed that velocity fields and anisotropy parameters are smooth. Thus, it is natural to apply a Laplacian operator to the parameter fields.

In Chapter 2 I review the properties of mode conversion and traditional approaches to velocity analysis of PS-waves. Also discussed is the PP+PS=SS method, which includes identification (registration) of PP and PS events from the same interfaces and computation of SS reflection data. Chapter 3 introduces my velocity-analysis methodology, which essentially represents joint tomography of the recorded PP- and generated SS-waves. In Chapter 4, the algorithm is first tested on a horizontal VTI

layer sandwiched between isotropic media and then on a layered model that includes a dipping reflector (e.g., a fault plane). The results confirm that if reflections from two different dips are available, the joint MVA can resolve the VTI parameters of piecewise-homogeneous models without additional information. Then the algorithm is tested on a more complex model with a laterally heterogeneous VTI syncline. In Chapter 5, the joint MVA is applied to a 2D section from 3D OBS (ocean bottom seismic) data acquired at Volve field in the North Sea. The conclusions and recommendations for future work are presented in Chapter 6.

CHAPTER 2
IMPLEMENTATION OF THE PP+PS=SS METHOD

P-wave reflection traveltimes generally are insufficient to resolve the parameters V_{P0} , ϵ , and δ (Thomsen, 1986) required for P-wave depth imaging in VTI media. Alkhalifah & Tsvankin (1995) showed that P-wave reflection traveltimes are fully controlled by only two parameters - the NMO velocity from a horizontal reflector $V_{\text{nmo}}(0)$ and the anellipticity coefficient η :

$$V_{\text{nmo}}(0) = V_0 \sqrt{1 + 2\delta}, \quad (2.1)$$

$$\eta = \frac{\epsilon - \delta}{1 + 2\delta} \quad . \quad (2.2)$$

Because the vertical velocity contributes to $V_{\text{nmo}}(0)$ only in combination with δ , P-wave traveltimes data cannot be used to resolve V_{P0} and determine the depth scale of VTI media. Therefore, to build a VTI model for prestack depth migration, at least one medium parameter (e.g., V_{P0}) must be known a priori (Sarkar & Tsvankin, 2004). In practice, one can use borehole information (e.g., well logs, check shots, or VSP data) to constrain parameter estimation.

As discussed in Tsvankin & Grechka (2000), combining P-wave traveltimes with the moveout of PS-waves converted at a horizontal and dipping interface can help constrain the vertical P- and SV-wave velocities and the parameters ϵ and δ . The most significant problem in PS-wave velocity analysis is the moveout asymmetry with respect to zero offset in CMP geometry (Tsvankin & Grechka, 2011). Unless the model is laterally homogeneous and has a horizontal symmetry plane, the PS traveltimes does not stay the same when the source and receiver are interchanged [i.e., $t_{PS}(x_1, x_2) \neq t_{PS}(x_2, x_1)$, where x_1 and x_2 are the source and receiver locations.].

Another feature of PS reflections is the polarity reversal near the zero-amplitude trace, which causes problems for semblance analysis and stacking. Converted-wave migration is more complicated than that for pure modes because the velocity fields for downgoing and upgoing rays are different. Therefore, most migration velocity analysis methods designed for pure modes cannot be directly applied to converted waves.

Migration velocity analysis for converted PS waves can be based on perturbation theory as the one developed by Liu (1997) for P-wave data. That method derives a quantitative relationship between residual moveout and velocity error (Donati & Stewart, 1998). In this approach, paraxial raytracing is performed to obtain traveltimes tables to be used in the prestack migration. For converted-wave migration, two traveltimes tables are needed. One of them is associated with downgoing P-waves and the other one to upgoing S-waves. The need for different velocity models for downgoing and upgoing waves significantly complicates migration velocity analysis.

Here, we employ the PP+PS=SS method (Grechka & Tsvankin, 2002b) to produce pure SS reflection events using PP and PS reflections from the same interface. We consider the application of the PP+PS=SS method in 2D case. Implementation of the method requires event registration or identification of PP and PS reflections from the same interfaces. Suppose PP- and PS-wave reflection data are acquired along a line in the dip direction of the subsurface structure and the vertical plane is a plane of symmetry. Then the reflected rays are confined to the incidence plane and the reflection traveltimes depends only on the in-plane velocity field. However, the PP+PS=SS method does not require knowledge of velocity.

After recording the PP and PS data, we sort them into common-receiver gathers (Figure 2.1). The horizontal slowness of a PP ray that travels from the source x_1 to the receiver x_2 can be evaluated at point x_1 as

$$P_{PP}(x_1, x_2) = \left. \frac{dt_{PP}(x, x_2)}{dx} \right|_{x=x_1}. \quad (2.3)$$

We can estimate the horizontal slowness of a PS ray in a similar way.

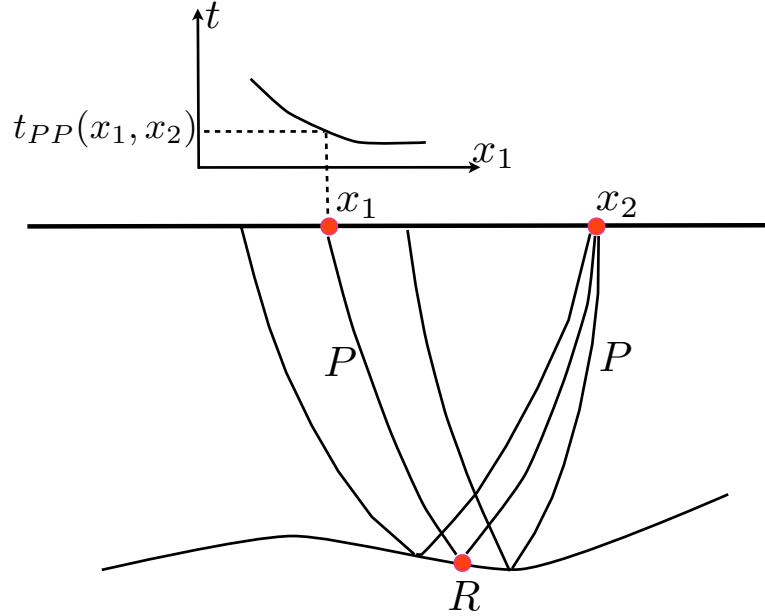


Figure 2.1: PP traveltimes recorded in a common-receiver gather (after Grechka and Tsvankin, 2002).

For a specific PP-wave source-receiver pair (x_1, x_2) , we search for the PS-wave traveling from x_1 to x_3 that has the same horizontal slowness at the source x_1 . Next, we switch the source and receiver position for the PP-wave and find the PS-wave excited at x_2 and recorded at x_4 , which has the same horizontal slowness as the PP-wave at source x_2 . Then the ray x_3Rx_4 corresponds to a pure SS reflection with the source and receiver positions at x_3 and x_4 with the traveltime given by

$$t_{SS}(x_3, x_4) = t_{PS}(x_1, x_3) + t_{PS}(x_2, x_4) - t_{PP}(x_1, x_2). \quad (2.4)$$

Hence, we can build a pure SS reflection by matching time slopes (horizontal slownesses) in common-receiver gathers of PP- and PS-waves (Figure 2.2).

While the constructed SS-wave traveltimes are exact, the PP+PS=SS method cannot produce correct reflection amplitudes. A “full-waveform” version of the PP+PS=SS method based on equation 2.4 was developed by Grechka & Dewangan (2003). They

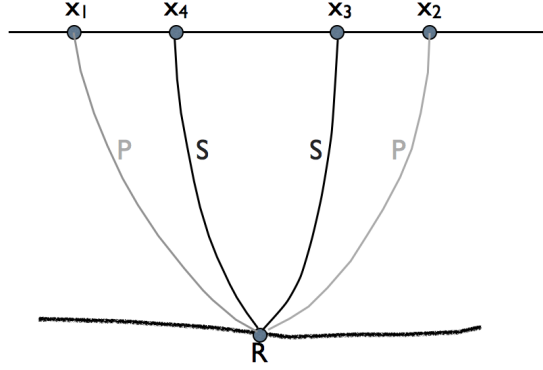


Figure 2.2: Matching the horizontal slownesses on common-receiver PP and PS sections at locations x_1 and x_2 helps find the source-receiver coordinates x_3 and x_4 of the pure SS ray x_3Rx_4 . This reconstructed SS ray has the same reflection point R as the PP ray x_1Rx_2 and PS rays x_1Rx_3 and x_2Rx_4 (after Grechka and Tsvankin, 2002).

apply a particular convolution of PP and PS traces to generate seismograms of the constructed SS-waves. The convolution operation in the frequency domain is given by

$$W_{SS}(\omega, x_3, x_4) = \int \int W_{PS}(\omega, x_1, x_3) W_{PP}^*(\omega, x_1, x_2) W_{PS}(\omega, x_2, x_4) dx_1 dx_2, \quad (2.5)$$

where ω is the radial frequency, W_{PP} and W_{PS} are the spectra of PP and PS traces, W_{SS} is the spectrum of the constructed SS trace for the source and receiver located at x_3 and x_4 , and “*” denotes complex conjugate. The integration is performed over all the P-wave source and receiver coordinates x_1 and x_2 and is therefore computationally expensive.

Hence, here I obtain the SS-waves by matching the PP- and PS-waves time slopes in common receiver gathers and then convolve the computed SS traveltimes with a Ricker wavelet to generate “pseudo” SS reflection data for MVA. The maximum reflection angle of the shear wave generated by mode conversion in a horizontal isotropic

layer with the P- and S-wave velocities V_P and V_S is $\theta_S^{\text{crit}} = \sin^{-1}(V_S/V_P)$, and the half-offset h_S (Figure 2.3) cannot exceed the critical value,

$$h_S^{\text{crit}} = D \tan \left[\sin^{-1} \left(\frac{V_S}{V_P} \right) \right], \quad (2.6)$$

where D is the thickness of the layer. For example, for a typical $V_S/V_P = 1/2$, the maximum half-offset is less than $0.6D$. Therefore, it is necessary to include long-offset PP and PS data to generate SS data suitable for robust velocity analysis. The offsets of the computed SS-wave are smaller than those of the acquired PP and PS data but may be sufficient for MVA if the survey includes offsets reaching two target depths.

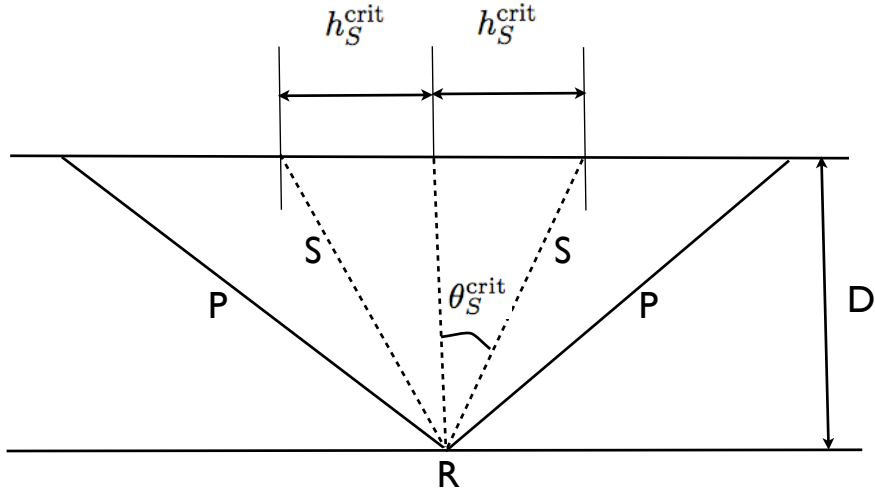


Figure 2.3: Critical (maximum) offset of the constructed SS-waves in a horizontal layer (Tsvankin & Grechka, 2011).

When matching the horizontal slownesses in common-receiver gathers of PP- and PS-waves, the choice of the threshold for equalizing time slopes is subjective and may result in missing data in the generated gathers (Figure 2.4). Therefore, we interpolate the computed SS data in CMP gathers to make them suitable for MVA (Figure 2.5).

We can better estimate the residual moveout after interpolation than in the unevenly sampled gathers.

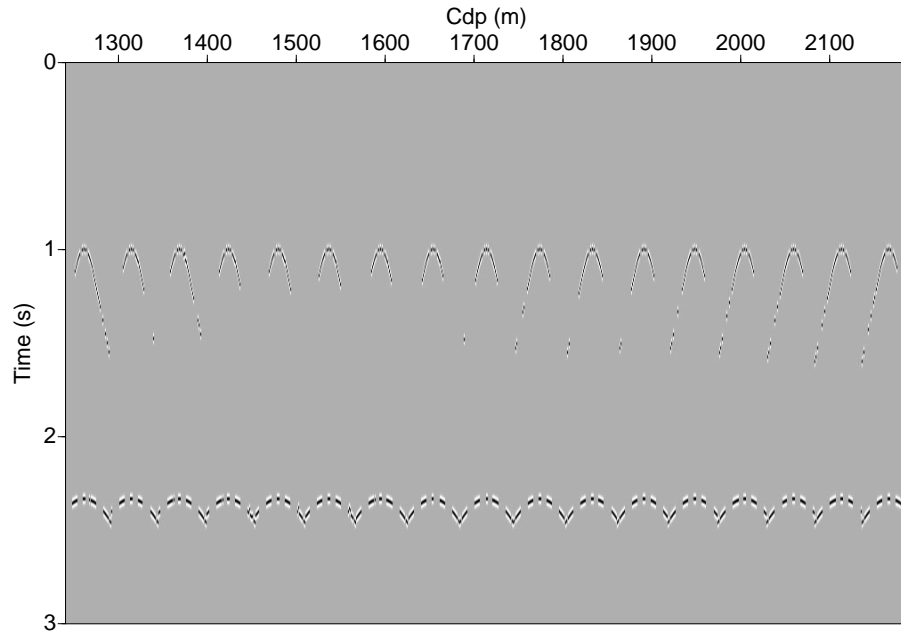


Figure 2.4: Constructed CMP gathers of SS-waves before interpolation.

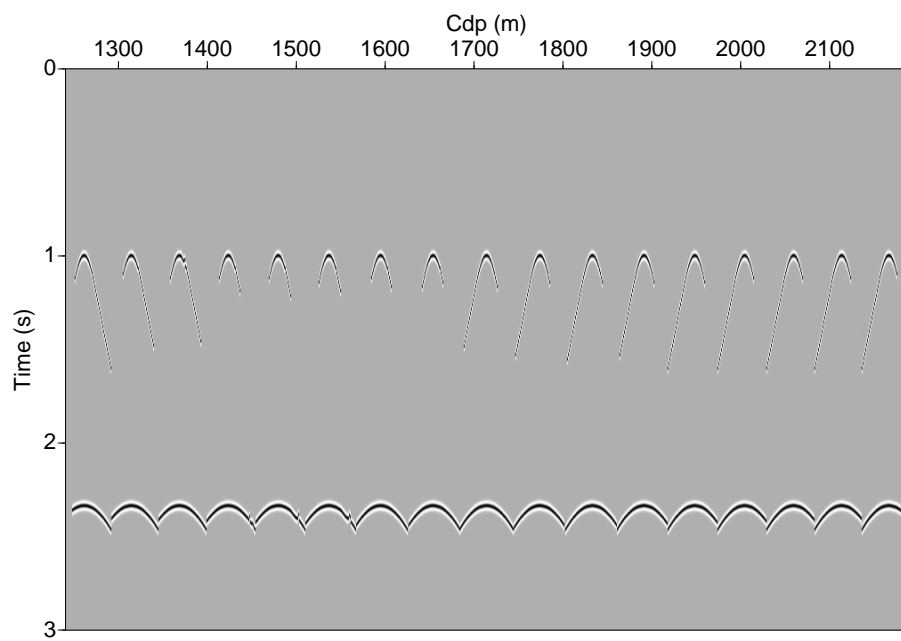


Figure 2.5: Gathers from Figure 2.4 after interpolation.

CHAPTER 3

2D JOINT MIGRATION VELOCITY ANALYSIS FOR VTI MEDIA

Reflection tomography recovers velocity models using information from migrated images. The tomographic parameter update is based entirely on the residual moveout of events in common image gathers. The velocity model is considered optimized when there is no residual moveout in CIG gathers. Otherwise, the velocity model is updated by minimizing the variance in the migrated depths of events in image gathers (flattening the moveout). The migrated depth z as a function of the half-offset h can be written as (Sarkar & Tsvankin, 2004):

$$z^2(h) = z^2(0) + Ah^2 + B \frac{h^4}{h^2 + z^2(0)}, \quad (3.1)$$

where z is the migrated depth, $z(0)$ is the zero-offset depth of the reflector and the coefficients A and B are found by a 2D semblance scan.

To apply equation 3.1 in migration velocity analysis, we need to pick an approximate value of $z(0)$ on the migrated section. A and B are found by maximizing the semblance value in image gathers. After estimating the residual moveout in CIGs, a derivative of the migrated depths with respect to the model parameters is computed. If λ represents a medium parameter, Sarkar & Tsvankin (2004) show that

$$\left[\frac{\partial \tau_s}{\partial z} + \frac{\partial \tau_r}{\partial z} \right] \frac{dz}{d\lambda} = - \left[\frac{\partial \tau_s}{\partial \lambda} - \frac{\partial \tau_r}{\partial \lambda} \right] \quad (3.2)$$

or

$$\frac{\partial z}{\partial \lambda} = - \left[\frac{\partial \tau_s}{\partial \lambda} - \frac{\partial \tau_r}{\partial \lambda} \right] \frac{1}{q_s + q_r}, \quad (3.3)$$

where $q_s = \frac{\partial \tau_s}{\partial z}$ and $q_r = \frac{\partial \tau_r}{\partial z}$ are the vertical slownesses evaluated at the diffractor for the specular rays connecting the diffractor with the source and the receiver, respectively.

The vector of the model parameters can be updated by solving the following linear system:

$$\mathbf{A}^T \mathbf{A} \Delta \boldsymbol{\lambda} = \mathbf{A}^T \mathbf{b}. \quad (3.4)$$

The matrix \mathbf{A} contains the derivatives of traveltime with respect to the medium parameters and $\Delta \boldsymbol{\lambda}$ is a vector composed of the parameter updates. The corresponding perturbation of the traveltime between the source and the diffractor is divided by the perturbation in $\boldsymbol{\lambda}$ to obtain $\partial \tau_s / \partial \boldsymbol{\lambda}$; and the same procedure is applied to find $\partial \tau_r / \partial \boldsymbol{\lambda}$.

For gridded tomography, the model is divided into square cells, and the parameters V_{P0} , ϵ , and δ are defined at each grid point. Because the number of unknowns is large, these derivatives are not obtained from traveltime differences caused by parameter perturbations but are computed analytically along the ray trajectory. According to Wang & Tsvankin (2012), the traveltime derivative with respect to the parameter $\boldsymbol{\lambda}$ is approximately given by

$$\frac{\partial \tau}{\partial \boldsymbol{\lambda}} = -\frac{\delta t}{V} \left(\frac{\partial V}{\partial \boldsymbol{\lambda}} \right), \quad (3.5)$$

where V is the P-wave phase velocity and δt is the time sample in ray tracing. Therefore, the traveltime derivatives with respect to the parameters can be expressed through the corresponding derivatives of the P-wave phase velocity.

Because inversion using P-wave reflection is nonunique, anisotropic models can be constrained by adding well information. The MVA algorithm of Wang & Tsvankin (2012) combines surface P-wave seismic data with borehole information to estimate model parameters that both flatten the CIGs and fit the walkaway VSP (vertical seismic profiling) traveltimes. VSP traveltimes are computed for each trial model and included in the following objective function \mathbf{F} :

$$\mathbf{F}(\Delta \boldsymbol{\lambda}) = \|\mathbf{A} \Delta \boldsymbol{\lambda} - \mathbf{b}\|^2 + \zeta_{vsp}^2 \|\mathbf{E} \Delta \boldsymbol{\lambda} - \mathbf{d}\|^2 + \mathbf{R}(\Delta \boldsymbol{\lambda}), \quad (3.6)$$

where the vector $\Delta\boldsymbol{\lambda}$ composed of the parameter updates $(\Delta V_{P0}, \Delta\epsilon, \Delta\delta)$ is defined at each grid point, the matrix \mathbf{E} includes VSP traveltime derivatives, the vector \mathbf{d} is the difference between the observed and calculated VSP traveltimes, and \mathbf{R} is a regularization operator. Because of the additional constraints from VSP data, the model parameters can often be estimated with sufficiently high accuracy.

Here, we extend the MVA algorithm of Wang & Tsvankin (2012) to multicomponent (PP and SS) data. Since we operate with PP- and SS-waves, the parameter set includes not just V_{P0} , ϵ , and δ , but also the shear-wave vertical velocity V_{S0} . The model is divided into square cells, and the parameters V_{P0} , V_{S0} , ϵ , and δ are defined at each grid point (Figure 3.1).

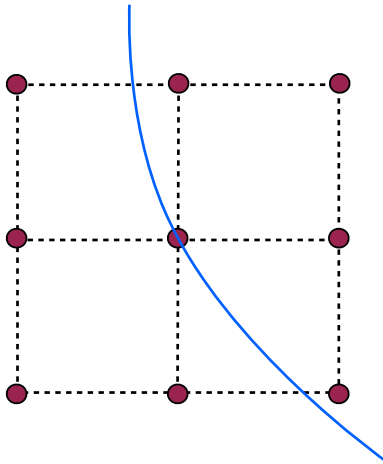
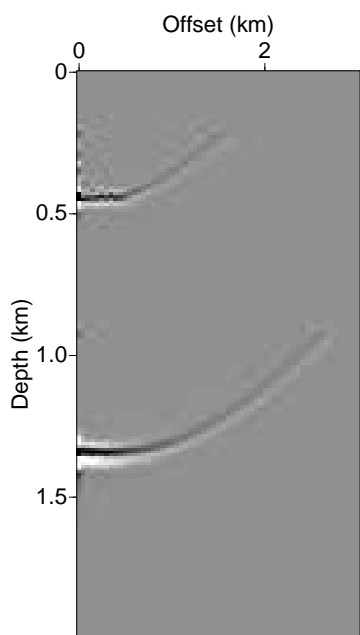
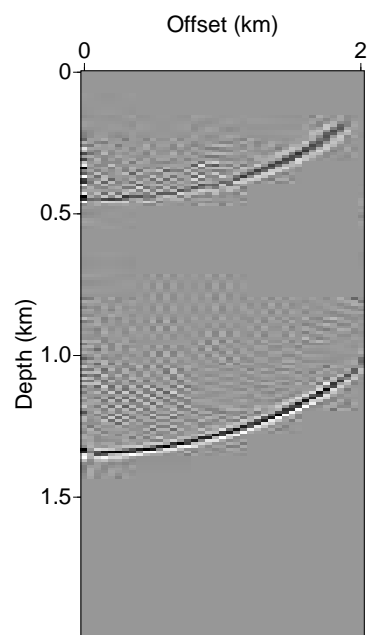


Figure 3.1: Gridded model for reflection tomography.

The moveouts in PP and SS CIGs (Figures 3.2(a) and 3.2(b)) serve as the input to joint MVA. The nonhyperbolic equation 3.1 is used to describe the moveout in PP CIGs. There is no need to apply equation 3.1 to SS-wave CIGs because the offset-to-depth ratio of the constructed SS events seldom exceeds 1-1.2. It is well known that



(a)



(b)

Figure 3.2: (a) PP-wave moveout and (b) SS-wave moveout.

the images of the same reflector using PP and SS reflections do not match in depth if the model parameters are incorrect. For the joint MVA, we not only minimize the residual moveout in PP and SS CIGs, but also perform codepthing, which involves tying PP and SS images of the same reflectors in depth. The objective function (see below) includes a term that penalizes the mismatch in depth of PP and SS migrated images using a selection of key reflection points (Figure 3.3). These points are chosen

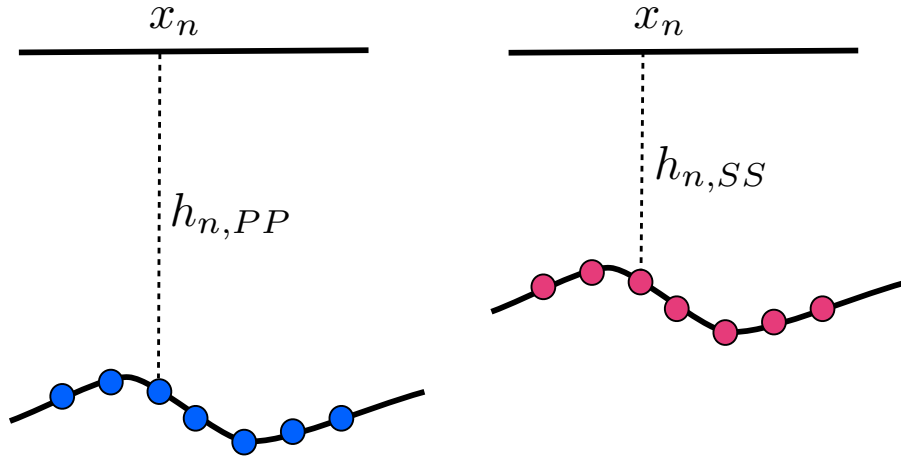


Figure 3.3: Reflection points may be imaged at different depths on PP and SS sections.

on the basis of coherency and focusing (Foss *et al.*, 2005).

To update model parameters, it is necessary to compute the P- and SV-wave phase velocity derivatives with respect to the model parameters (Wang & Tsvankin, 2012). The exact P- and SV-wave phase velocities in VTI media can be expressed as (Tsvankin, 2005):

$$\begin{aligned} \frac{V^2}{V_{P0}^2} &= 1 + \epsilon \sin^2 \theta - \frac{f}{2} \\ &\pm \frac{f}{2} \sqrt{1 + \frac{4 \sin^2 \theta}{f} (2\delta \cos^2 \theta - \epsilon \cos 2\theta) + \frac{4\epsilon^2 \sin^4 \theta}{f^2}}, \end{aligned} \quad (3.7)$$

where θ is the phase angle with the symmetry axis and $f \equiv 1 - \frac{V_{S0}^2}{V_{P0}^2}$. The plus in front of the radical corresponds to P-waves and the minus to S-waves. For purposes of MVA, however, it is convenient to replace ϵ and δ with the P-wave horizontal ($V_{\text{hor,P}}$) and NMO ($V_{\text{nmo,P}}$) velocities given by $V_{\text{hor,P}} = V_{P0}\sqrt{1+2\epsilon}$ and $V_{\text{nmo,P}} = V_{P0}\sqrt{1+2\delta}$. We compute the traveltime derivatives with respect to $V_{\text{hor,P}}$ and $V_{\text{nmo,P}}$ instead of ϵ and δ . The MVA algorithm updates V_{P0} , V_{S0} , $V_{\text{hor,P}}$, and $V_{\text{nmo,P}}$ and then converts $V_{\text{hor,P}}$ and $V_{\text{nmo,P}}$ into ϵ and δ . Assuming the updates are sufficiently small, we use the following matrix for conversion of the parameter updates:

$$\begin{pmatrix} \Delta V_{P0} \\ \Delta V_{S0} \\ \Delta V_{\text{hor,P}} \\ \Delta V_{\text{nmo,P}} \end{pmatrix} = \begin{pmatrix} 1 & & & \\ & 1 & & \\ & & V_{P0} & \\ & & & V_{P0} \end{pmatrix} \begin{pmatrix} \Delta V_{P0} \\ \Delta V_{S0} \\ \Delta \epsilon \\ \Delta \delta \end{pmatrix}.$$

The objective function used in the joint MVA is as follows:

$$\begin{aligned} F(\Delta\lambda) &= \mu_1 \|\mathbf{A}_P \Delta\lambda + \mathbf{b}_P\|^2 + \mu_2 \|\mathbf{A}_S \Delta\lambda + \mathbf{b}_S\|^2 \\ &+ \mu_3 \|\mathbf{D} \Delta\lambda + \mathbf{y}\|^2 + \zeta \|L \Delta\lambda\|^2, \end{aligned} \quad (3.8)$$

where \mathbf{A}_P and \mathbf{A}_S depend on the derivatives of the PP and SS migrated depths with respect to the medium parameters, the vectors \mathbf{b}_P and \mathbf{b}_S contain elements that characterize the residual moveout in PP- and SS-wave CIGs, the matrix \mathbf{D} describes the differences between the derivatives of the PP and SS migrated depths with respect to the medium parameters, and the vector \mathbf{y} contains the differences between the migrated depths on the PP and SS sections. The full definitions of \mathbf{A}_P , \mathbf{A}_S , \mathbf{D} , \mathbf{b}_P , \mathbf{b}_S , and \mathbf{y} are given in Appendix A.

Minimizing the first two terms ($\|\mathbf{A}_P \Delta\lambda + \mathbf{b}_P\|^2$ and $\|\mathbf{A}_S \Delta\lambda + \mathbf{b}_S\|^2$) allows us to flatten PP and SS CIGs. Codepthing is achieved through minimizing the third term ($\|\mathbf{D} \Delta\lambda + \mathbf{y}\|^2$). Because the tomographic inversion can be ill-posed, we add a regularization term ($\|L \Delta\lambda\|^2$) to the objective function. The coefficients μ_1 , μ_2 , μ_3

and ζ govern the weights of the corresponding terms.

The objective function is minimized by a least-squares algorithm. The VTI parameters are updated at each grid point, making the inversion time-consuming. To improve computational efficiency, the algorithm is written to take advantage of parallel computing. Common-image gathers for each reflector are computed on different processors, and flattening of PP and SS events is performed simultaneously.

CHAPTER 4

SYNTHETIC TESTS

We use anisotropic ray-tracing package ANRAY (Gajewski & Pšencík, 1987) to compute PP- and PS-wave reflection traveltimes for synthetic tests. ANRAY is developed by the consortium project “Seismic Waves in Complex 3D Structures” (SW3D) at Charles University in Prague. PP and SS images are generated with Kirchhoff prestack depth migration (Seismic Unix program ‘sukdmig2d’). To create traveltime tables of PP- and SS-waves, we perform ray tracing for heterogeneous VTI media using SU code ‘rayt2dan’.

4.1 Models composed of homogeneous layers

We first test the MVA algorithm on a simple horizontally layered model (Figure 4.1) that includes a VTI layer sandwiched between isotropic media. Without dipping interfaces, the interval parameters for this model cannot be constrained solely by PP and PS reflection traveltimes (Grechka & Tsvankin, 2002a; Tsvankin & Grechka, 2011). Therefore, the P-wave vertical velocity V_{P0} is assumed to be known, and we invert only for V_{S0} and the anisotropy parameters ϵ and δ of the VTI layer.

The top layer is known to be isotropic and its P- and S-wave velocities can be easily found from reflection data. The initial S-wave vertical velocity in the middle VTI layer is 10% smaller than the true value, and both ϵ and δ are set to zero. The maximum offset-to-depth ratio for the bottom of the VTI layer is close to two, which is sufficient for applying the PP+PS=SS method. Indeed, the maximum offset for the constructed SS data is 1.6 km, and the corresponding offset-to-depth ratio exceeds unity. The entire PP data set is used along with the SS-waves to estimate the residual moveout in CIGs. For codepthing, however, we only use conventional-spread PP data with offsets not exceeding those for the constructed SS-waves.

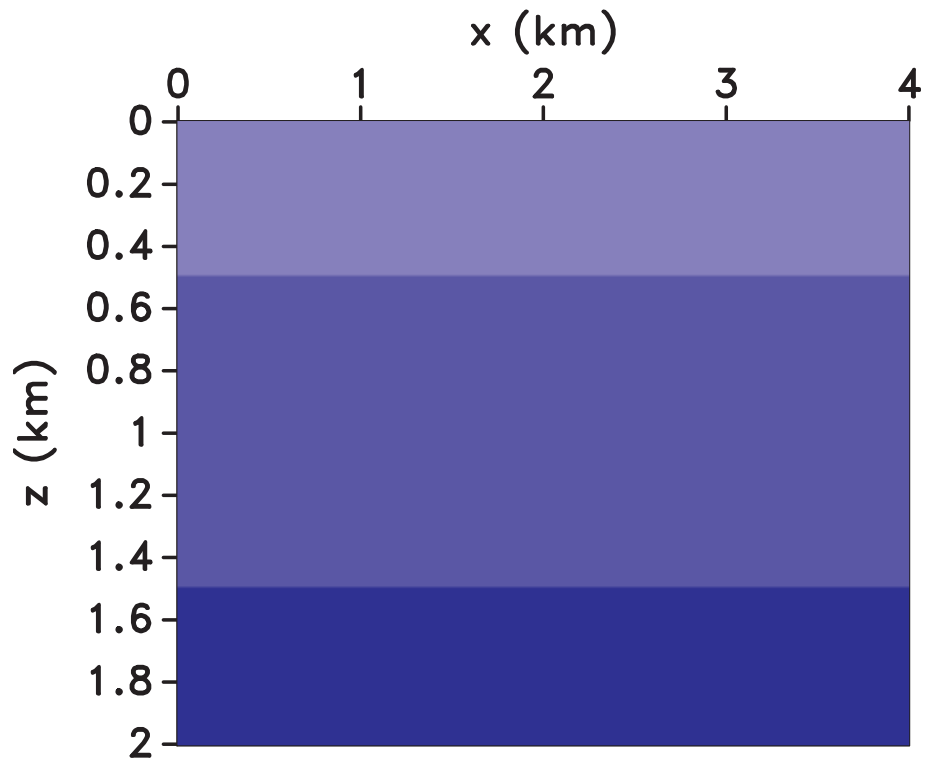


Figure 4.1: Model with a VTI layer embedded between two isotropic layers. The P- and S-wave velocities in the top layer are $V_P = 2000$ m/s and $V_S = 1000$ m/s; for the second layer, $V_{P0} = 3000$ m/s, $V_{S0} = 1500$ m/s, $\epsilon = 0.1$, and $\delta = -0.1$.

The initial PP and SS depth images are generated with Kirchhoff prestack depth migration. The PP and SS image gathers are not flat (Figures 4.2(a) and 4.2(b)), and

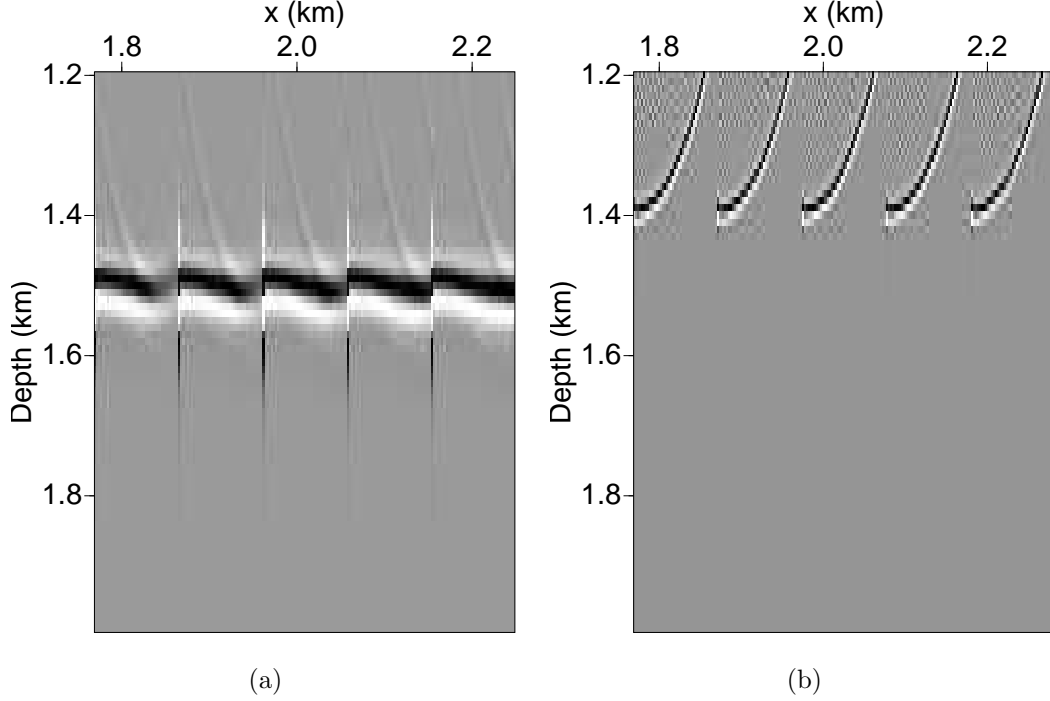


Figure 4.2: Common-image gathers of (a) PP-waves and (b) SS-waves (displayed every 100 m) after migration with the initial model.

the bottom of the VTI layer is not only poorly focused but also imaged at different depths on the PP and SS sections (Figures 4.3(a) and 4.3(b)). CIGs used for velocity analysis are uniformly sampled from 1 km to 3 km along the second reflector.

Since we use gridded tomography, the derivatives of migrated depths with respect to the model parameters are calculated at the vertices of relatively fine grids. Therefore, we follow Wang & Tsvankin (2012) in employing a mapping matrix to convert the model updates into the parameter values at each grid point. After 10 iterations, the CIGs are flat (Figures 4.4(a) and 4.4(b)) and the reflectors are tied in depth (Figures 4.5(a) and 4.5(b)). The estimated parameters of the VTI layer are close to the actual values: $V_{S0} = 1494$ m/s, $\epsilon = 0.1$, and $\delta = -0.09$ (V_{P0} is known).

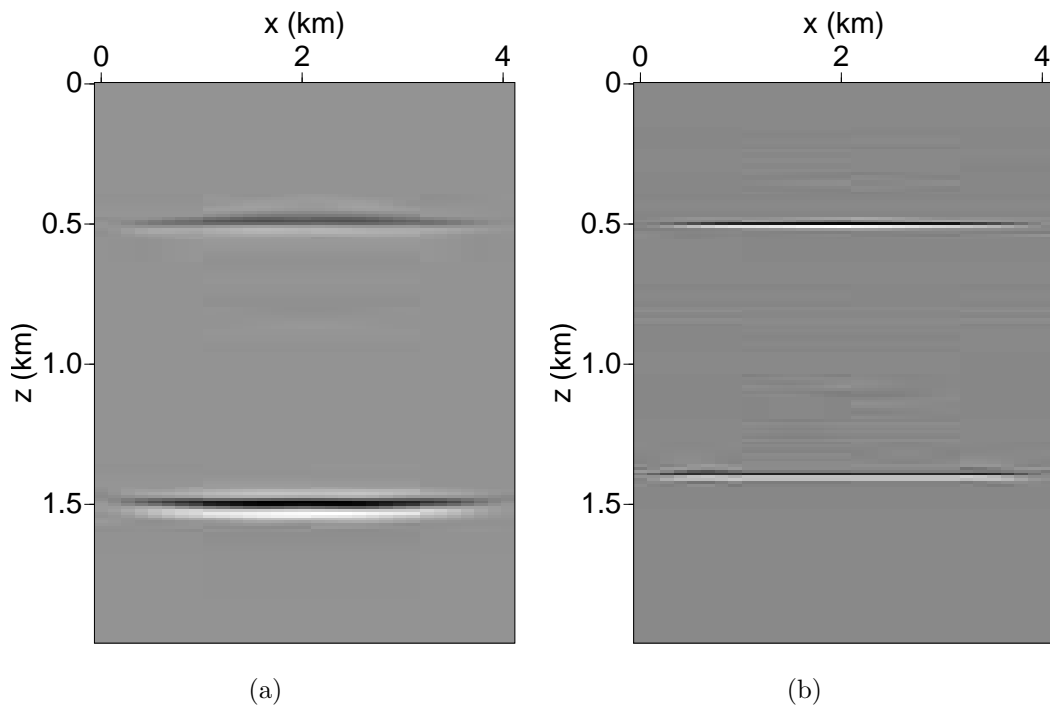


Figure 4.3: (a) PP-wave and (b) SS-wave depth images computed with the initial model.

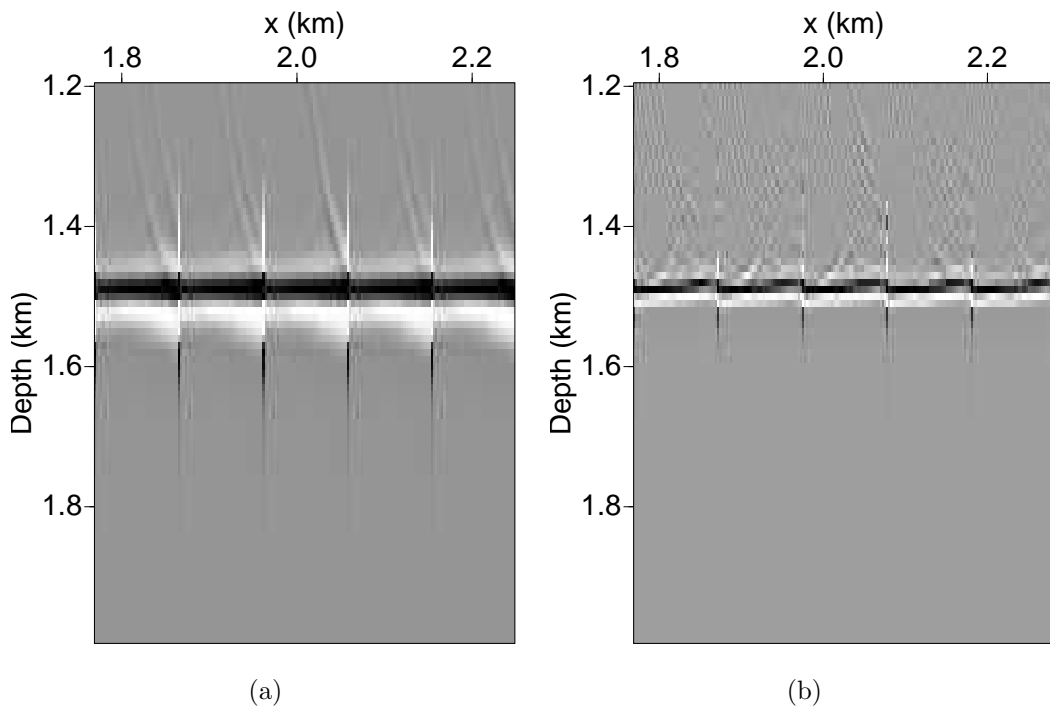


Figure 4.4: CIGs of (a) PP-waves and (b) SS-waves after migration with the inverted model.

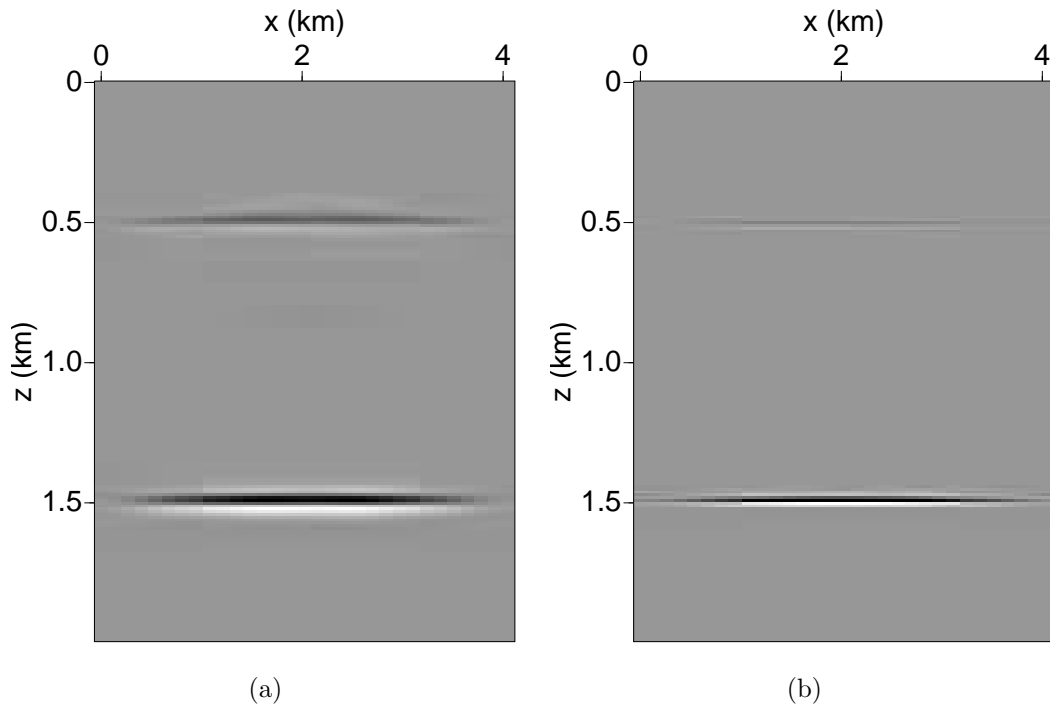


Figure 4.5: Final depth images of (a) PP-waves and (b) SS-waves with the inverted parameters for the model in Figure 4.1.

Next, the algorithm is tested on a model (Figure 4.6) that includes a reflector (e.g., a fault plane) dipping at an angle approaching 30° . To avoid instability in ray tracing, we smooth the corner of the dipping interface using bicubic spline interpolation. The synthetic data include PP and PS reflections from both horizontal and dipping reflectors (Figures 4.7(a), 4.7(b) and 4.7(c)). The maximum offsets are 4 km for PP data and 2 km for the SS-waves constructed by the PP+PS=SS method. Tsvankin & Grechka (2000) demonstrate that the traveltimes of the PP- and PS-waves reflected from a horizontal and a dipping interface are sufficient to constrain the parameters V_{P0} , V_{S0} , ϵ , and δ .

Assuming the velocities in the subsurface layer to be known, we invert for the parameters of the middle VTI layer. The initial model is isotropic with the velocities V_{P0} and V_{S0} distorted by 15%. The initial V_{P0}/V_{S0} ratio, which can be accurately estimated from the zero-offset traveltimes, was correct. The CIGs and depth sections

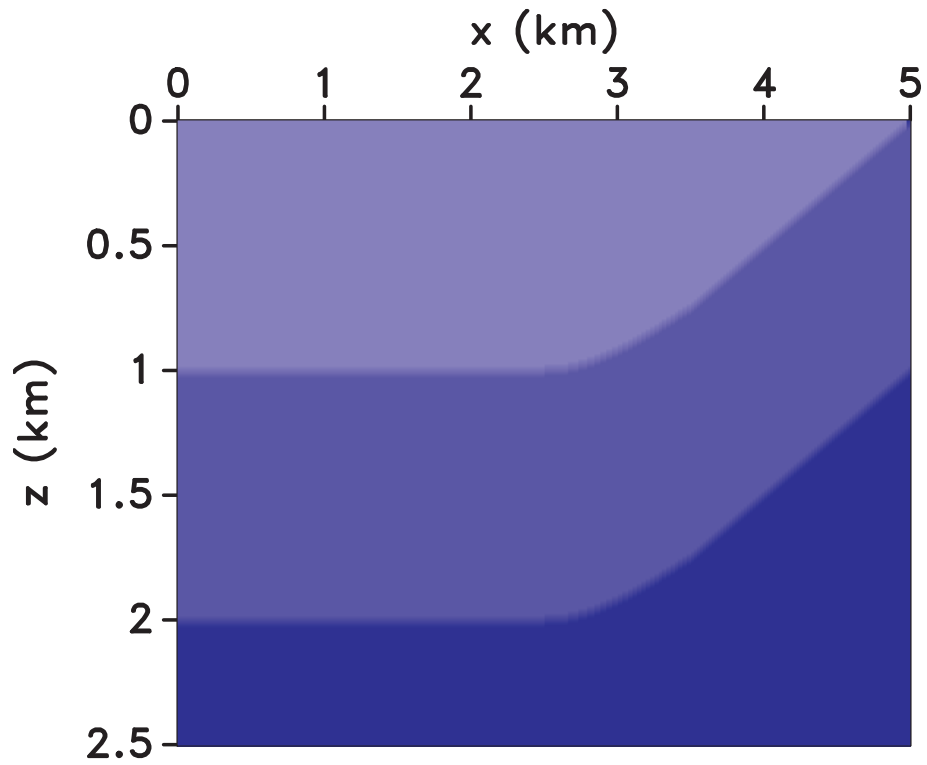


Figure 4.6: Three-layer model with dipping interfaces. The parameters of the first isotropic layer are $V_P = 2000$ m/s, $V_S = 1000$ m/s; for the second VTI layer, $V_{P0} = 3000$ m/s, $V_{S0} = 1500$ m/s, $\epsilon = 0.2$, and $\delta = 0.1$. The maximum dip of both reflectors is 27° .

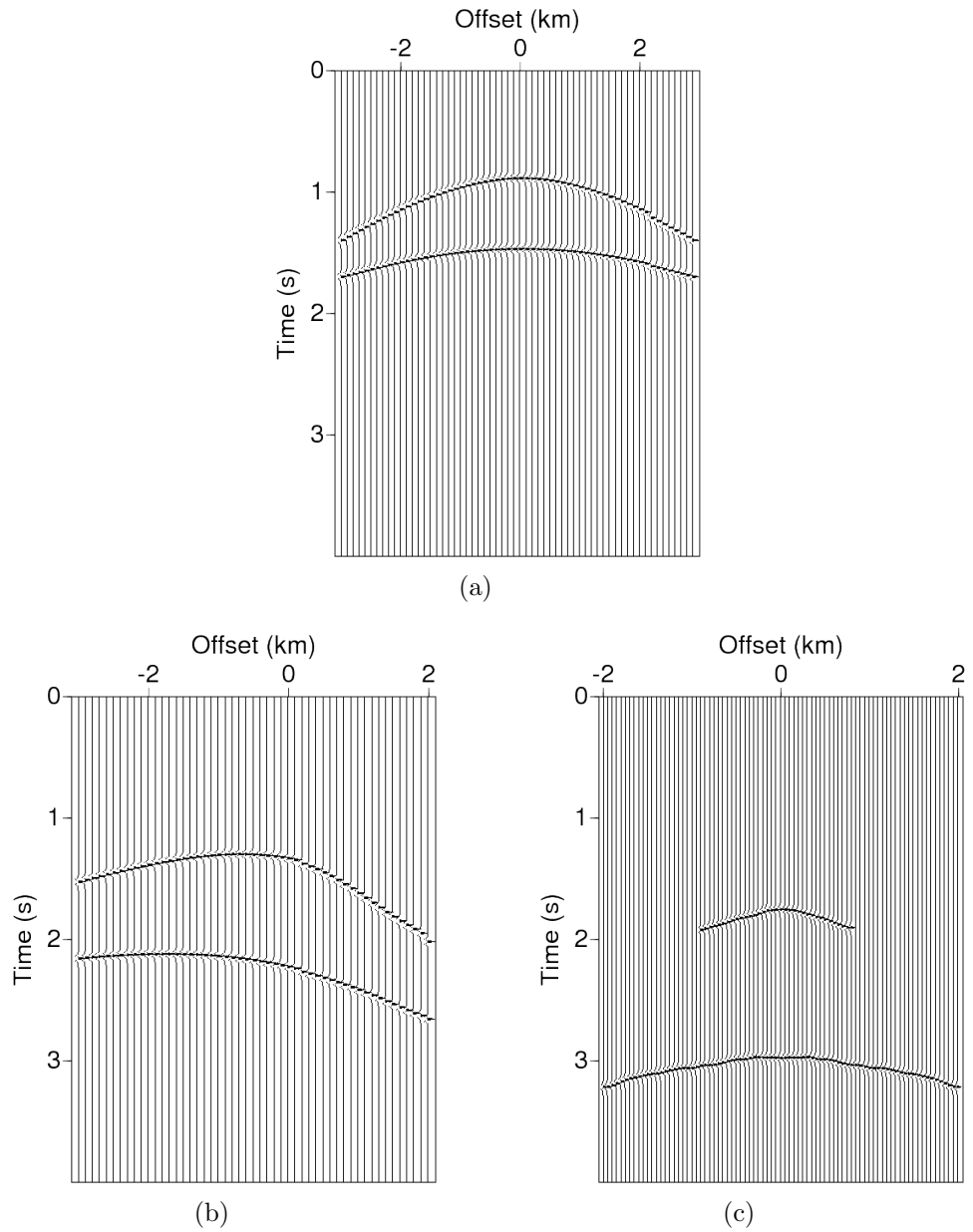


Figure 4.7: CMP gathers of the recorded (a) PP-waves and (b) PS-waves at location 3000 m. (c) The SS data constructed by the PP+PS=SS method at the same location.

computed with the initial model are displayed in Figures 4.8 and 4.9. A set of CIGs of PP- and SS-waves from both the horizontal and dipping interfaces (for locations from 1 km to 4 km) are used in the joint MVA.

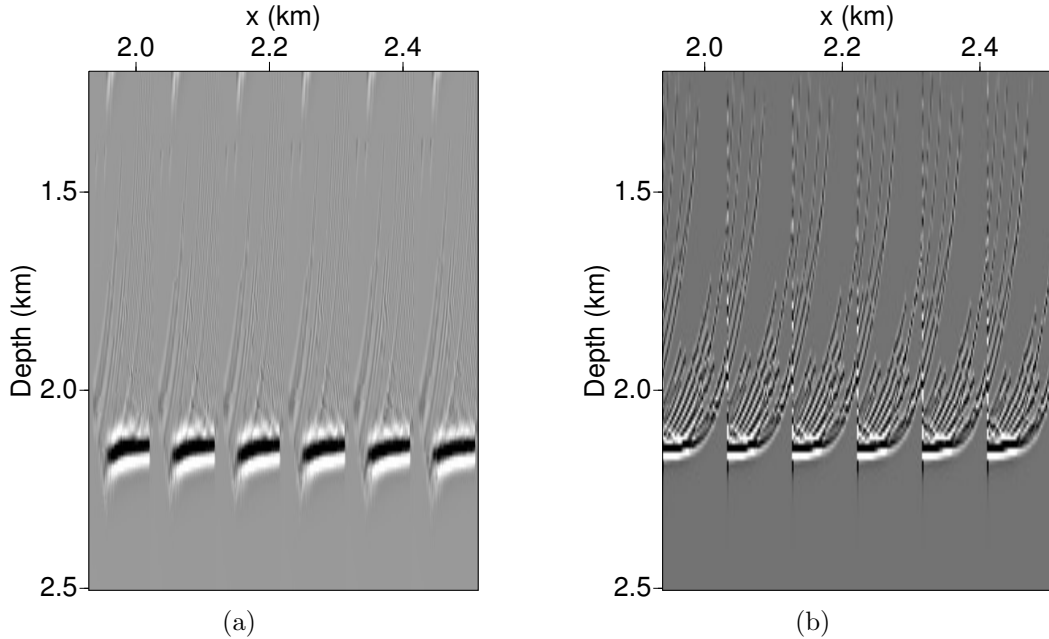


Figure 4.8: Common-image gathers of (a) PP-waves and (b) SS-waves (displayed every 100m) after migration with the initial model.

After 11 iterations, the algorithm practically removes residual moveout (Figures 4.10(a) and 4.10(b)) and the reflectors on the PP and SS sections are correctly positioned (Figures 4.11(a) and 4.11(b)). These results confirm the feasibility of building layered VTI depth models using 2D PP and PS reflection data if both horizontal and dipping events are available. The inversion also produces accurate estimates of the interval VTI parameters: $V_{P0} = 3031$ m/s, $V_{S0} = 1515$ m/s, $\epsilon = 0.20$, and $\delta = 0.08$.

4.2 Model with heterogeneous layers

It is important to assess the ability of the algorithm to reconstruct spatial velocity variations along with the anisotropy parameters. Following Sarkar & Tsvankin (2004), we build a model with a factorized VTI layer, in which the ratios of the stiffness

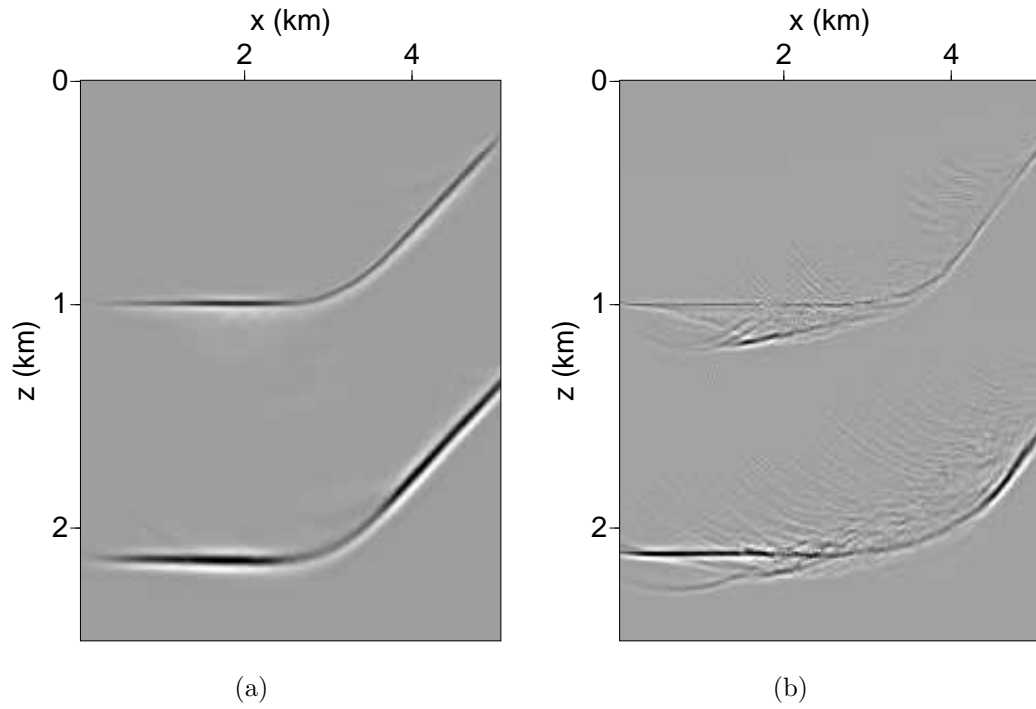


Figure 4.9: (a) PP-wave and (b) SS-wave depth images computed with the initial model.

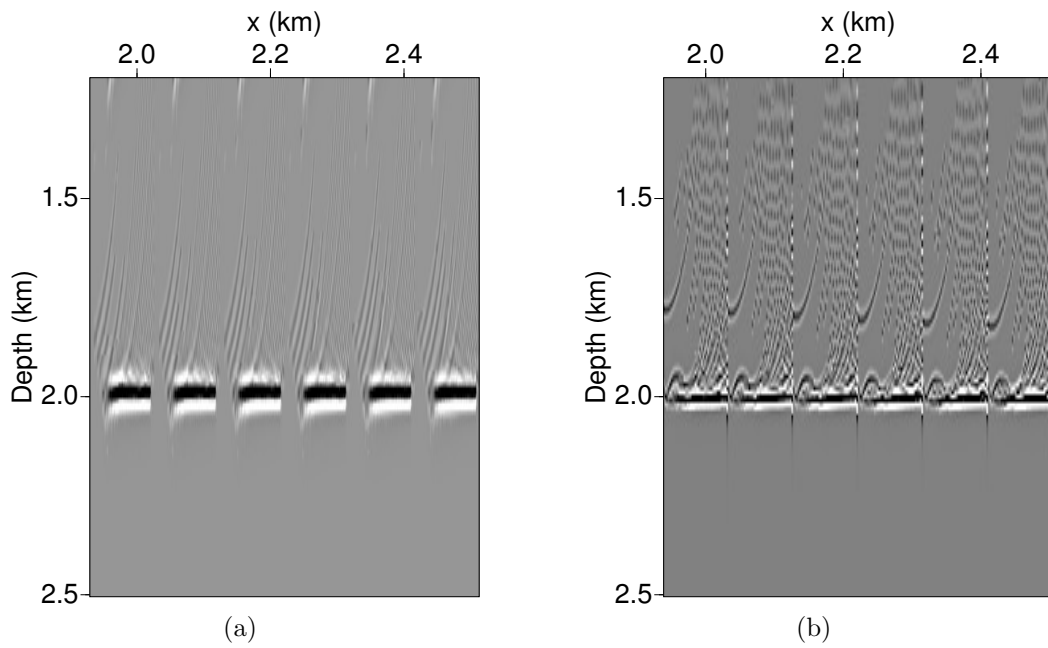


Figure 4.10: CIGs of (a) PP-waves and (b) SS-waves after migration with the inverted model.

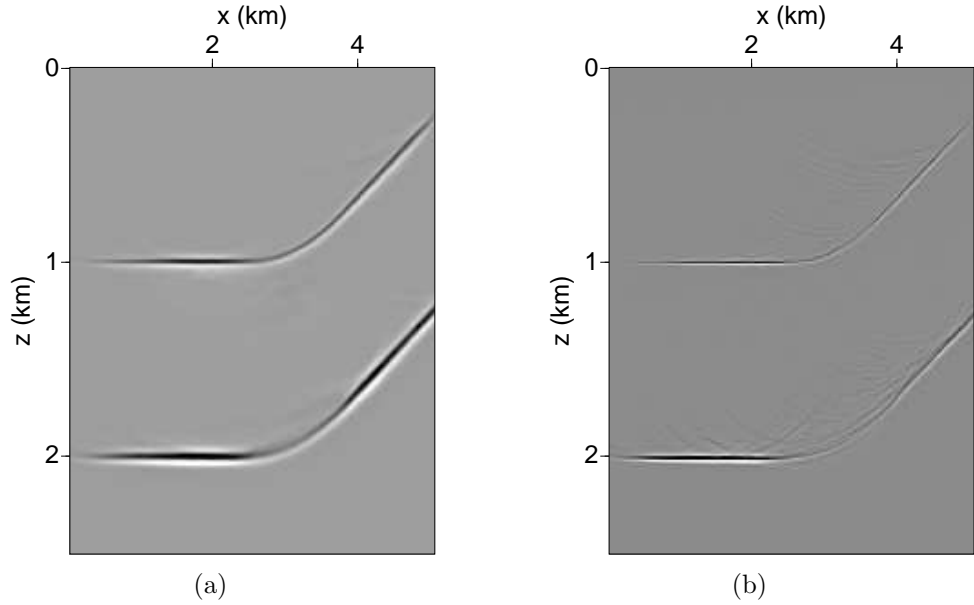


Figure 4.11: Final depth images of (a) PP-waves and (b) SS-waves obtained with the inverted parameters for the model in Figure 4.6.

coefficients (and, therefore, the anisotropy parameters and the V_{P0}/V_{S0} ratio) are constant (Figure 4.12). The vertical velocities in the VTI layer vary linearly in space, with V_{P0} defined as

$$V_{P0}(x, z) = V_{P0}(x_0, z_0) + k_{p,x}(x - x_0) + k_{p,z}(z - z_0), \quad (4.1)$$

where (x_0, z_0) is an arbitrary point inside the layer, and $k_{p,x}$ and $k_{p,z}$ are the lateral and vertical gradients, respectively. Because the VTI layer is factorized, the velocity V_{S0} at each point is obtained by setting $V_{P0}(x, z)/V_{S0}(x, z) = 2$. The dip of the flanks of the syncline is about 27° , and the VTI layer contains an additional internal reflector. The P- and S-wave velocities in the top layer (known to be isotropic) can be obtained from PP and SS traveltimes. In the inversion, we do not assume the VTI layer to be fully factorized, but the anisotropy coefficients inside it are kept constant. Also, in the first test, both V_{P0} and V_{S0} are taken to be linear functions of x and z , so V_{S0} is described by

$$V_{S0}(x, z) = V_{S0}(x_0, z_0) + k_{s,x}(x - x_0) + k_{s,z}(z - z_0). \quad (4.2)$$

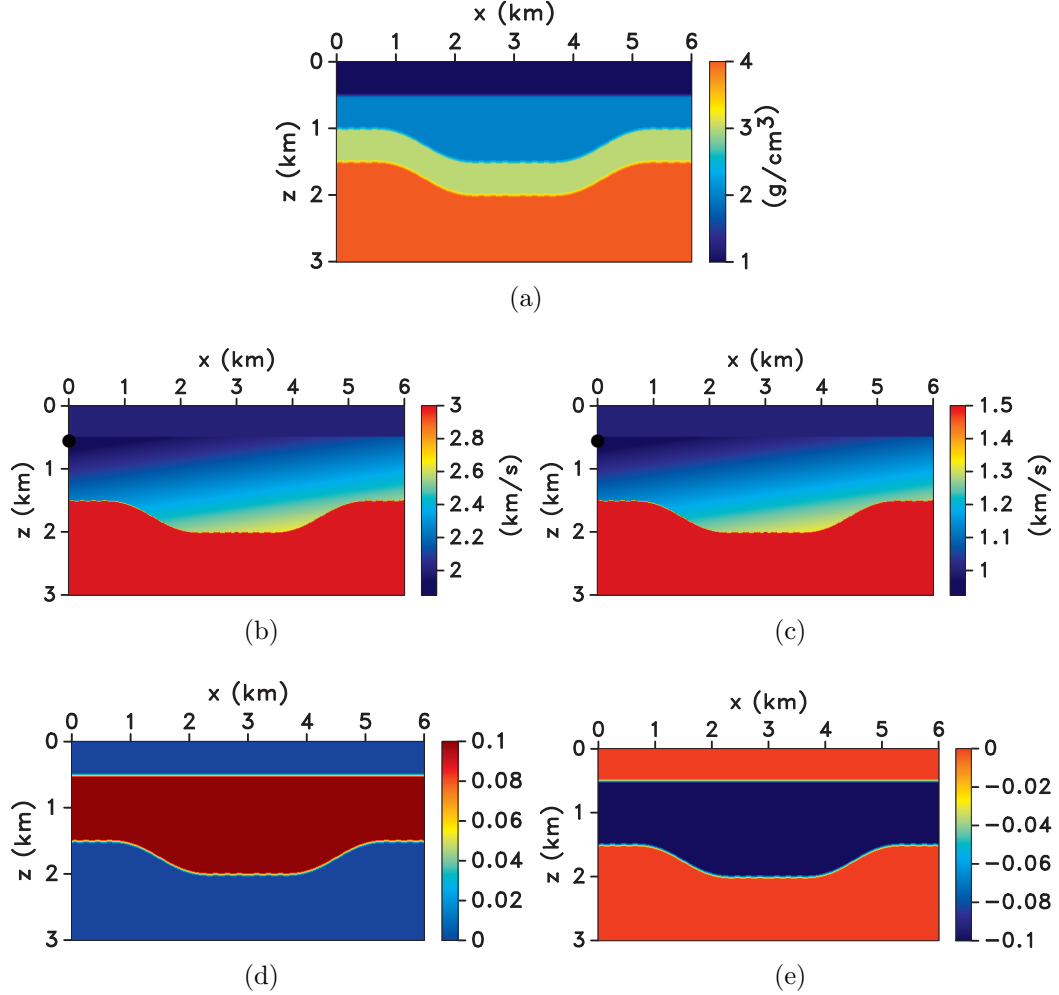


Figure 4.12: Model with a factorized VTI layer embedded between two isotropic homogeneous layers. (a) The density, the vertical velocities (b) V_{P0} and (c) V_{S0} , and the anisotropy parameters (d) ϵ and (e) δ . The parameters of the top layer are $V_P = 2000$ m/s and $V_S = 1000$ m/s. For the second layer, the vertical velocities at the point marked by a black dot on the left are $V_{P0} = 1850$ m/s and $V_{S0} = 925$ m/s. Both V_{P0} and V_{S0} vary linearly with the lateral gradients $k_{p,x} = 0.05\text{s}^{-1}$ and $k_{s,x} = 0.025\text{s}^{-1}$ and vertical gradients $k_{p,z} = 0.4\text{s}^{-1}$ and $k_{s,z} = 0.2\text{s}^{-1}$ so that $V_{P0}/V_{S0} = 1/2$. The anisotropy parameters of the VTI layer are constant: $\epsilon = 0.1$ and $\delta = -0.1$.

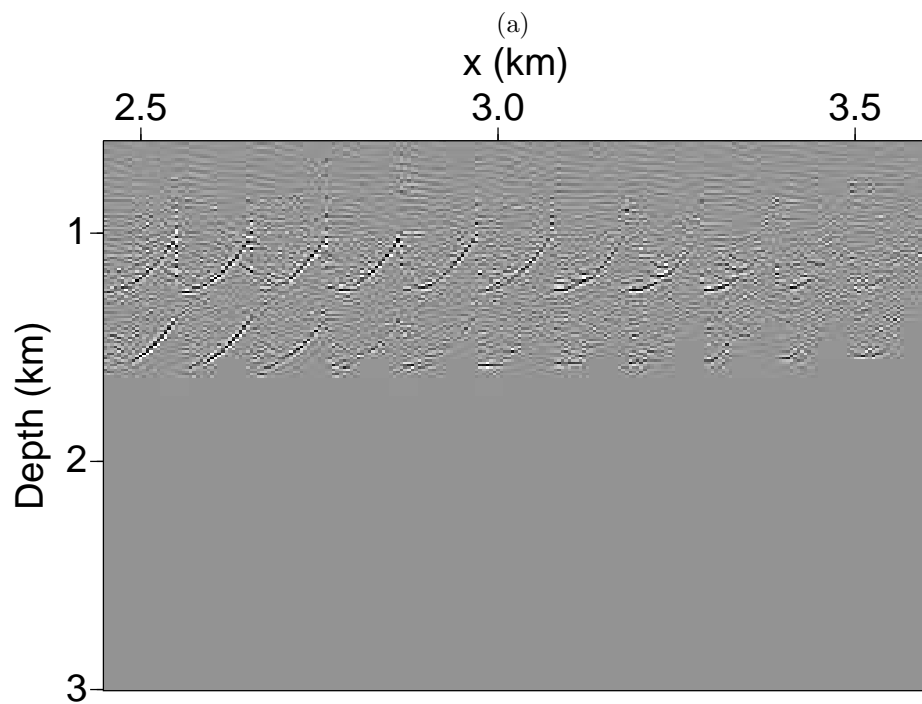
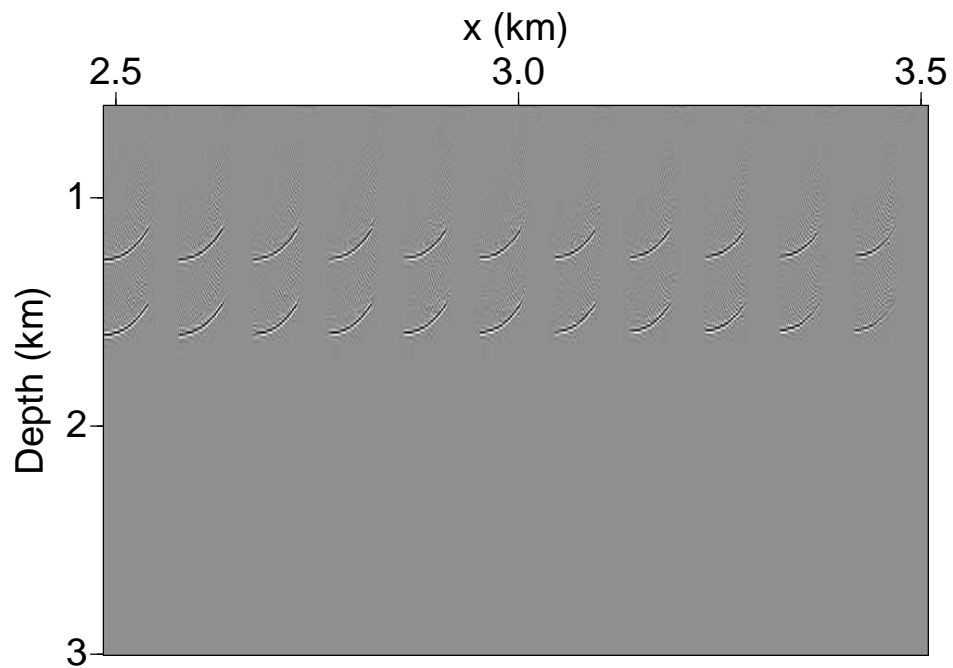
The algorithm inverts for the parameters $V_{P0}(x_0, z_0)$, $V_{S0}(x_0, z_0)$, k_x^P , k_z^P , k_x^S , k_z^S , ϵ and δ of the VTI layer.

The initial velocities V_{P0} and V_{S0} at the top of the middle layer (at the point marked by a black dot) are 10% smaller than the actual values, and k_x^P , k_z^P , k_x^S , k_z^S , ϵ , and δ of the initial model are set to zero. The PP- and SS-wave CIGs for the two reflectors in the VTI layer are not flat (Figures 4.13(a) and 4.13(b)), and these reflectors imaged with the initial model are poorly focused and shifted in depth (Figures 4.14(a) and 4.14(b)). Velocity analysis is performed for common-image gathers from 1 km to 5 km, including both the left and right flanks of the syncline. The maximum offset-to-depth ratio for the PP-wave CIGs is close to two, and it reduces to unity for the gathers of SS-waves.

After application of MVA to the two reflectors in the VTI layer, both PP and SS image gathers are flattened (Figures 4.15(a) and 4.15(b)), and PP and SS sections (Figures 4.16(a) and 4.16(b)) are tied in depth. Making the correct (linear) assumption about V_{P0} and V_{S0} and keeping ϵ and δ constant helped resolve all four relevant VTI parameters (Table 4.1).

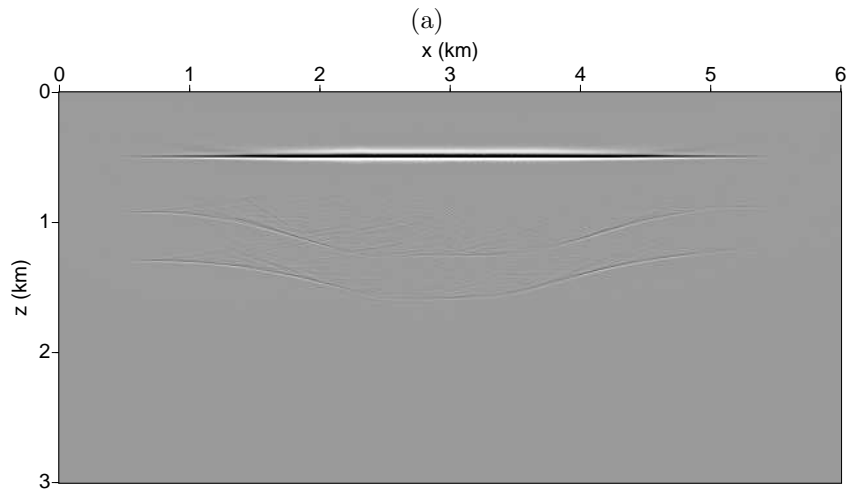
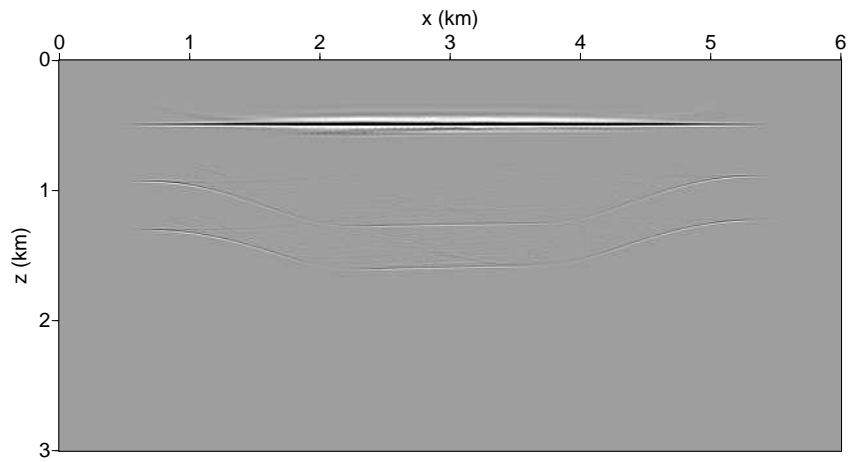
Table 4.1: Inversion results for the VTI layer from the model in Figure 4.12. The velocities V_{P0} and V_{S0} are correctly assumed to vary linearly inside the layer, and ϵ and δ are spatially invariant.

Model parameters	V_{P0} (m/s)	V_{S0} (m/s)	ϵ	δ
Actual	1850	925	0.1	-0.1
Initial	1665	833	0	0
Inverted	1873	945	0.11	-0.11
Error	1%	2%	0.01	-0.01
Model parameters	$k_x^P(s^{-1})$	$k_z^P(s^{-1})$	$k_x^S(s^{-1})$	$k_z^S(s^{-1})$
Actual	0.05	0.4	0.025	0.2
Initial	0	0	0	0
Inverted	0.043	0.42	0.023	0.21
Error	-14%	5%	-8%	5%



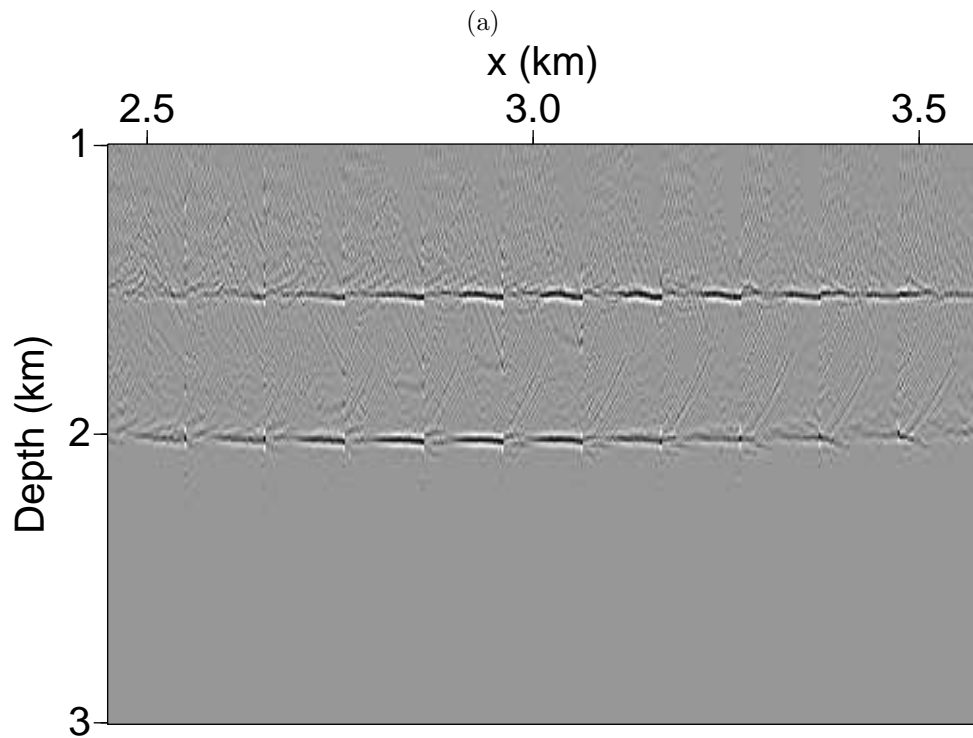
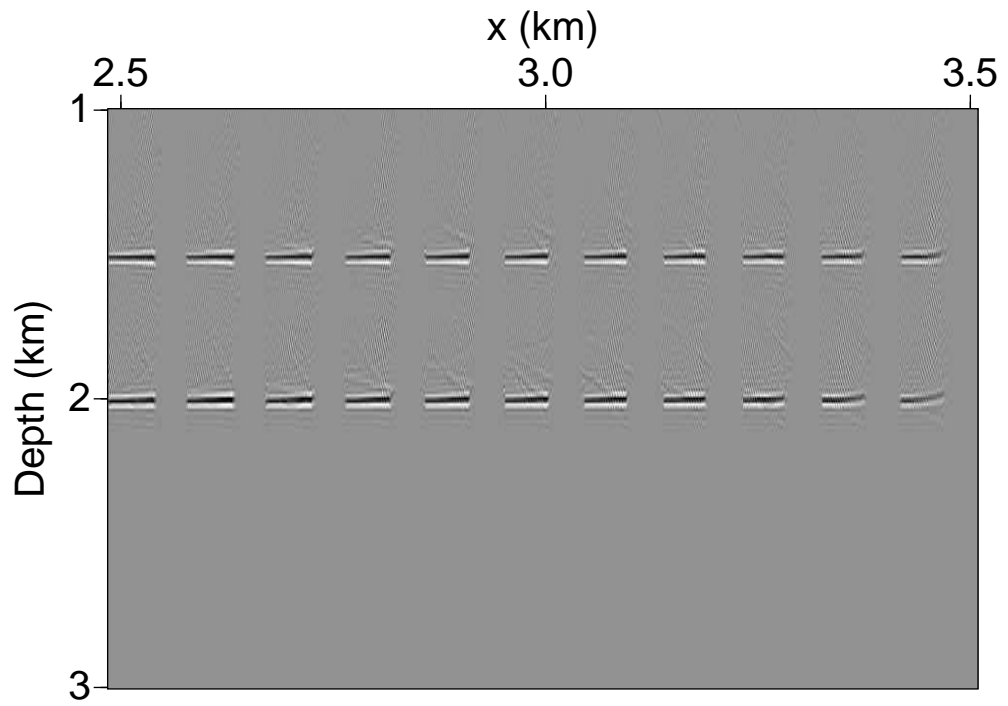
(b)

Figure 4.13: Common-image gathers of (a) PP-waves and (b) SS-waves (displayed every 100m) after migration with the initial model.



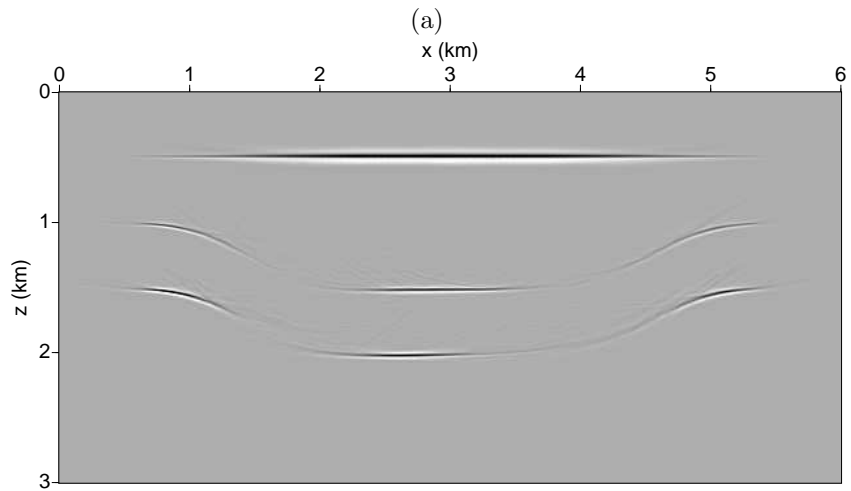
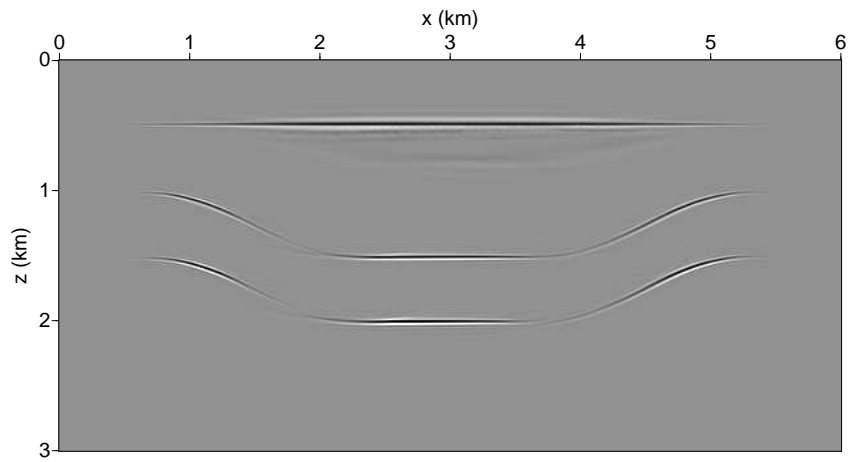
(b)

Figure 4.14: (a) PP-wave and (b) SS-wave depth images computed with the initial model.



(b)

Figure 4.15: CIGs of (a) PP-waves and (b) SS-waves after migration with the inverted model.

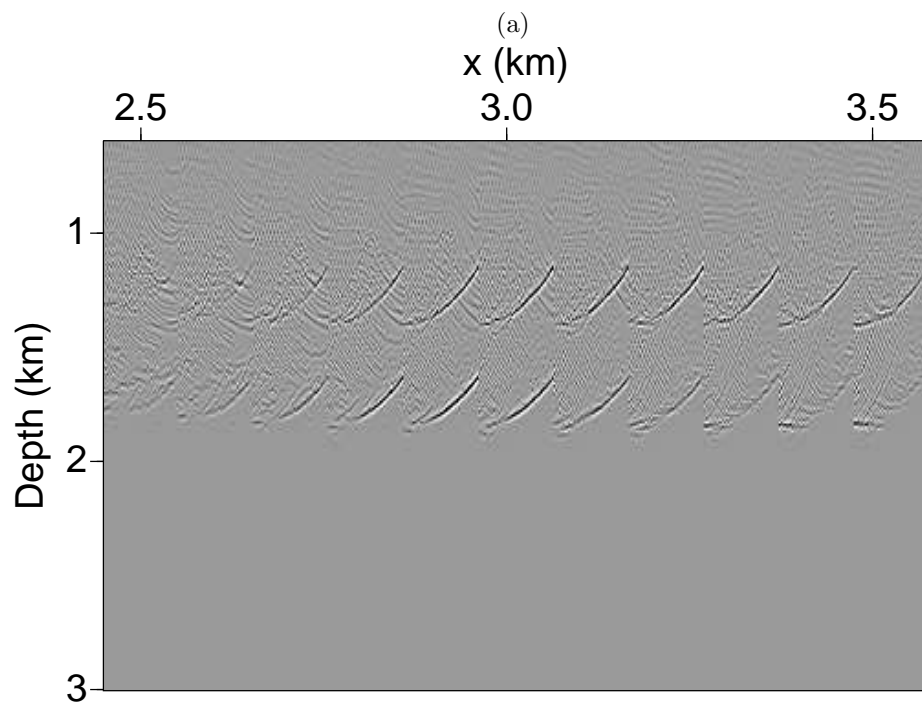
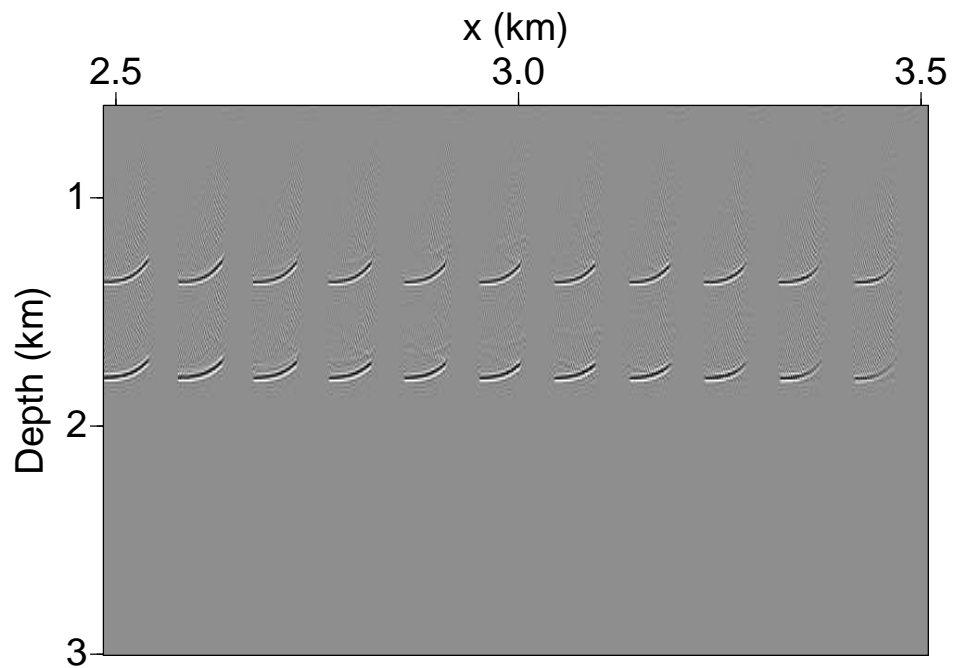


(b)

Figure 4.16: (a) PP-wave and (b) SS-wave depth images computed with the inverted parameters for the model in Figure 4.12.

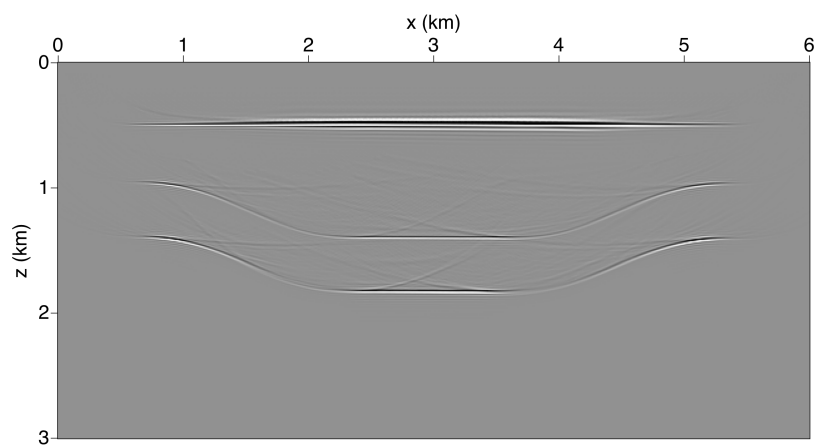
In the next test, the velocities V_{P0} and V_{S0} are updated at each grid point with no a priori constraints. However, the anisotropy parameters ϵ and δ in the VTI layer are still taken constant (i.e., spatially invariant). The regularization term $\|\mathbf{L}\Delta\lambda\|$ applied in inversion (equation 3.8) is a finite-difference approximation of the Laplacian.

The initial fields of V_{P0} and V_{S0} are obtained by reducing the actual values by 12% and 8%, respectively, and ϵ and δ are set to zero. As a result, CIGs are strongly distorted (Figure 4.17) and reflectors in the VTI layer are shifted up and are somewhat deformed (Figure 4.18). Also there is a mistie between the migrated PP and SS images at the bottom of the VTI layer. After nine iterations, joint tomography of PP- and PS-waves accurately reconstructs the parameter fields (Figure 4.19) and accomplishes the goal of flattening the image gathers (Figure 4.20) and minimizing the depth misties (Figures 4.21(a) and 4.21(b)). In particular, the mistie at the bottom of the VTI layer is reduced from 60 m to 5 m (Figure 4.22). However, the quality of the final images (Figures 4.21(a) and 4.21(b)) are not as high as those of the final sections in the previous test (Figures 4.16(a) and 4.16(b)) because of less restrictive model assumptions. We found that for laterally heterogeneous models the contribution of codelthing must be given a larger weight in the objective function during the last few iterations, whereas the first several updates can be mostly governed by flattening-related terms.

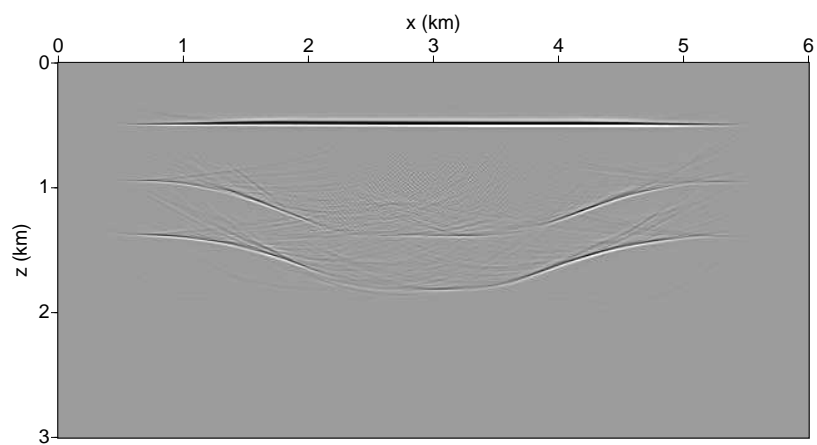


(b)

Figure 4.17: Common-image gathers of (a) PP-waves and (b) SS-waves (displayed every 100m) after migration with the initial model.



(a)



(b)

Figure 4.18: (a) PP-wave and (b) SS-wave depth images computed with the initial model parameters.

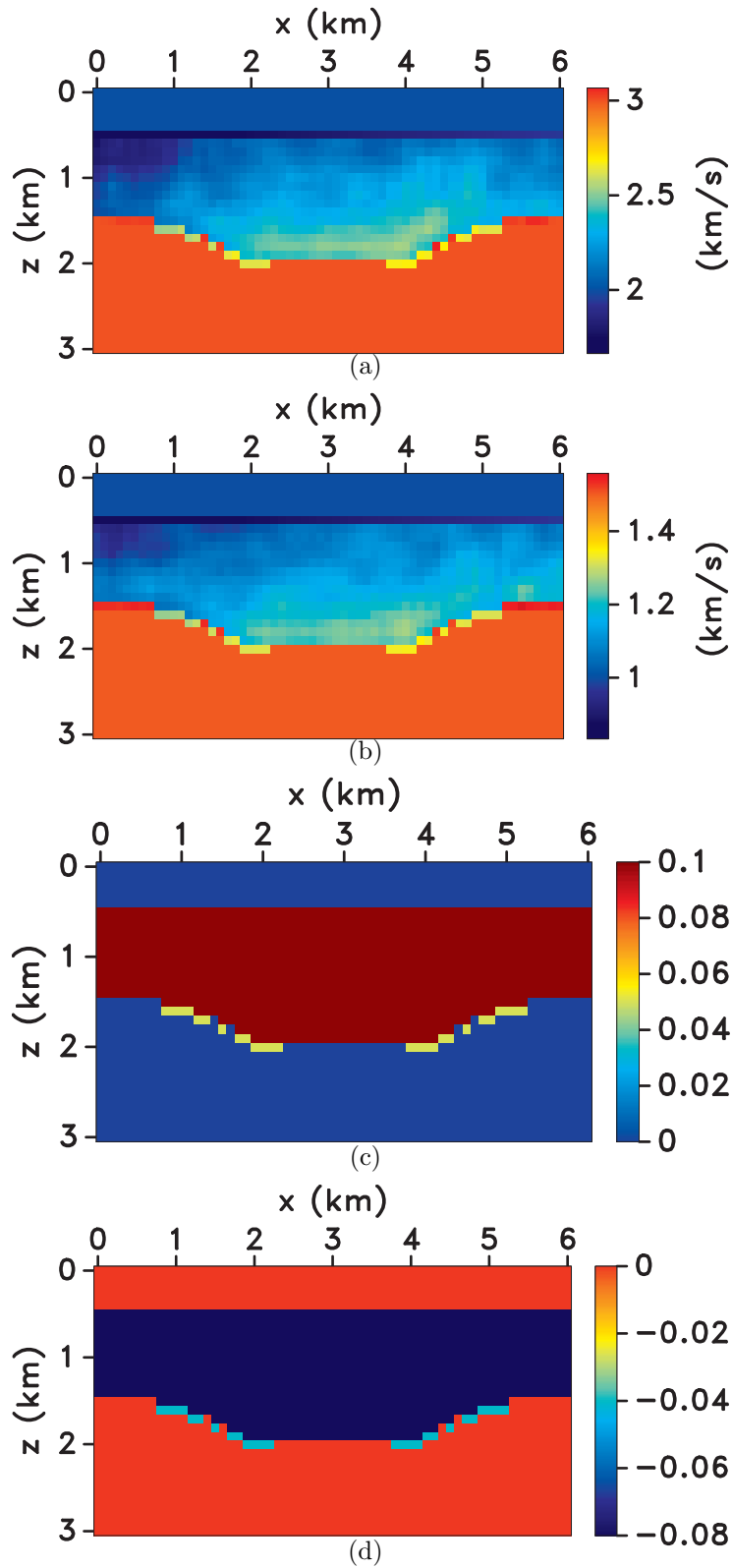
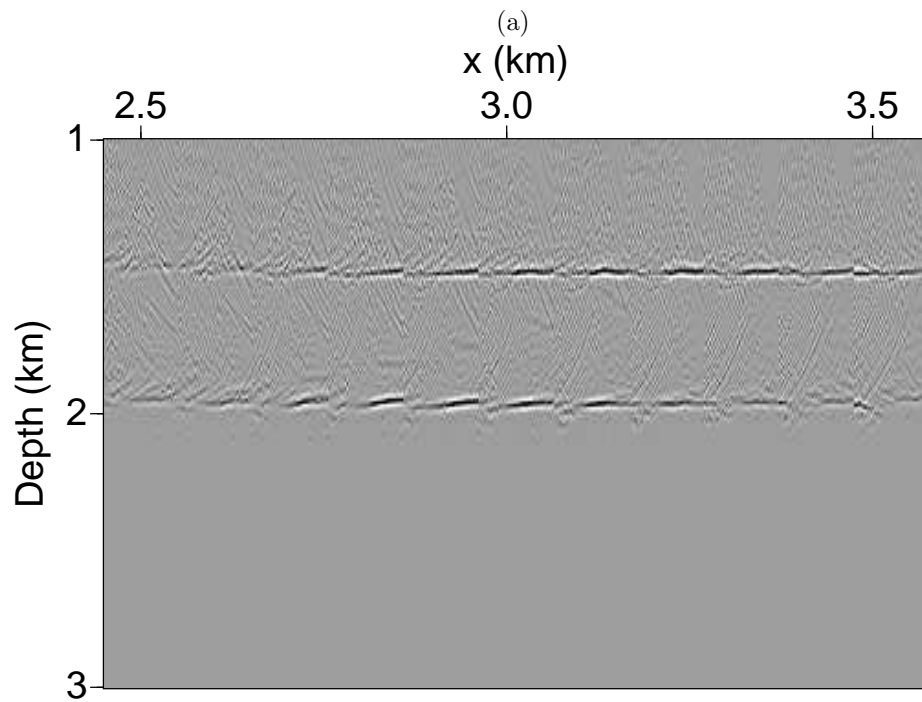
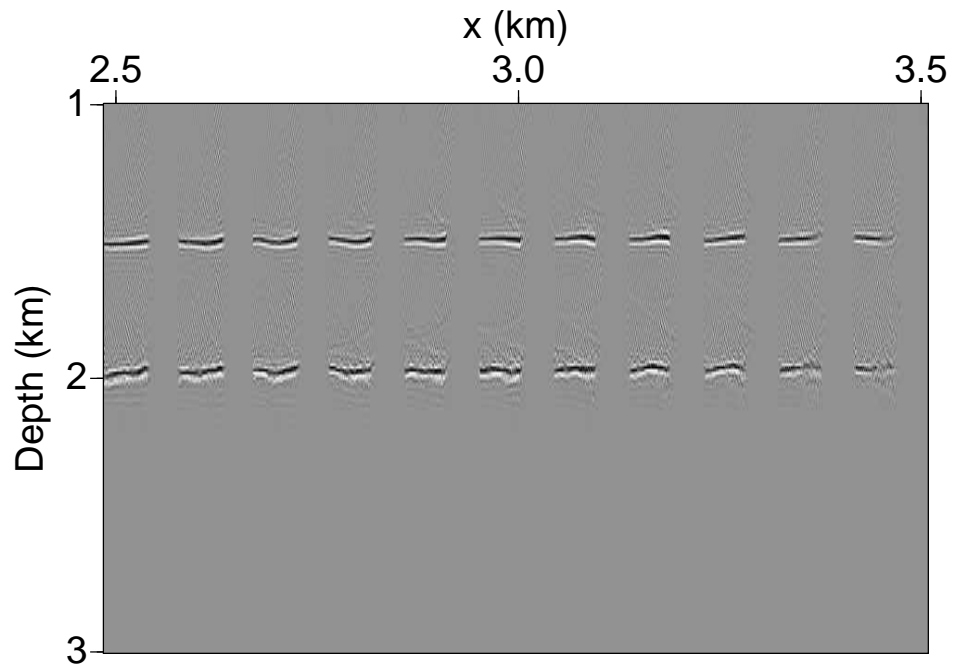
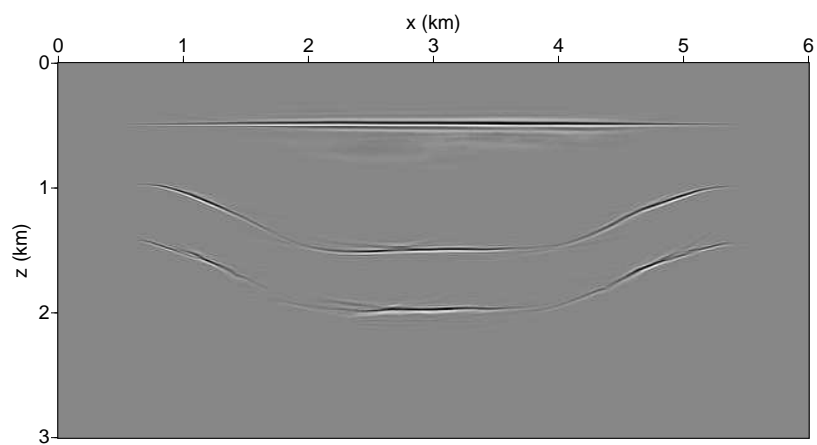


Figure 4.19: Velocities (a) V_{P0} and (b) V_{S0} for the model in Figure 4.12 estimated on a grid. Inverted layer-based parameters (c) ϵ and (d) δ .

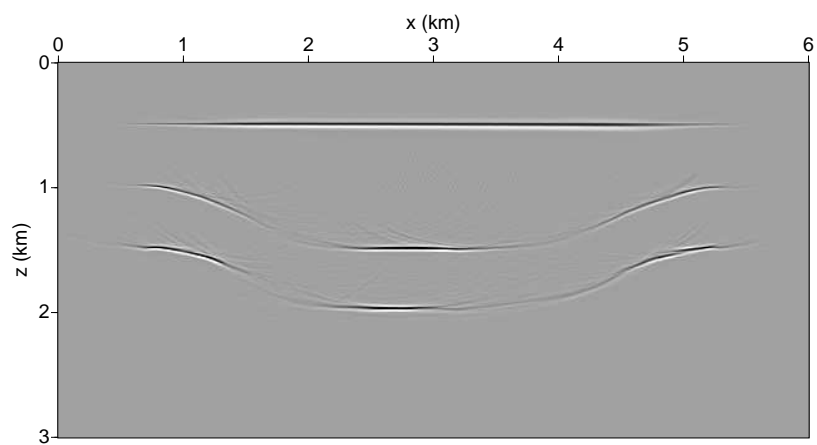


(b)

Figure 4.20: Common-image gathers of (a) PP-waves and (b) SS-waves (displayed every 100m) after migration with the estimated model.



(a)



(b)

Figure 4.21: (a) PP-wave and (b) SS-wave depth images computed with the estimated model parameters.

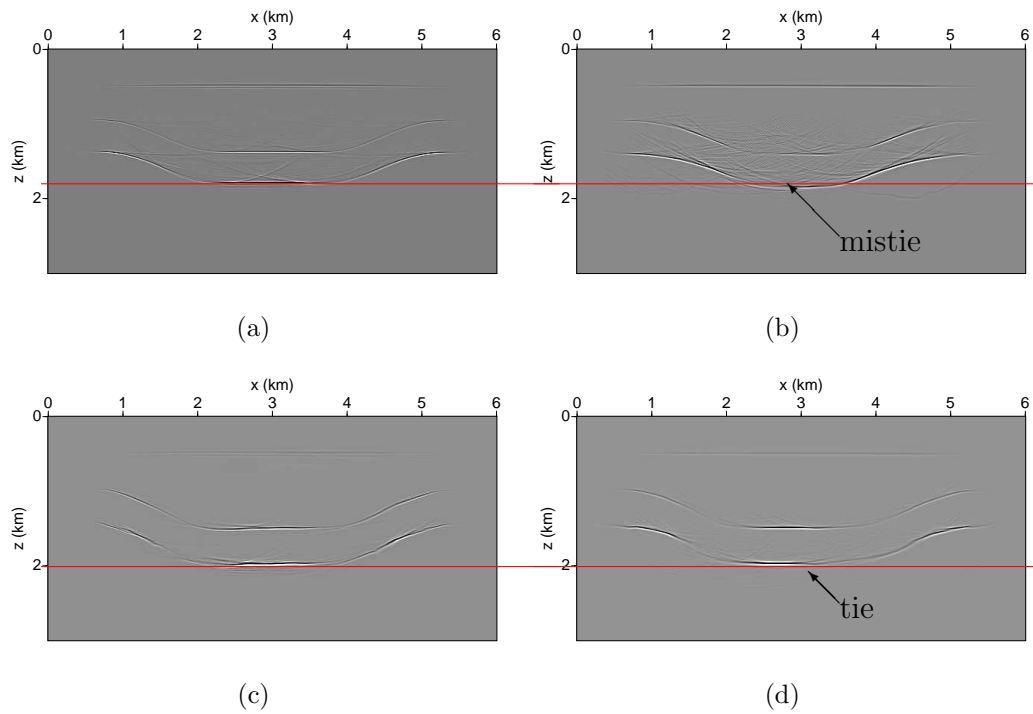


Figure 4.22: Depth mistie between the initial (a) PP-wave and (b) SS-wave images. The (c) PP-wave and (d) SS-wave images computed with the inverted model are tied in depth.

CHAPTER 5

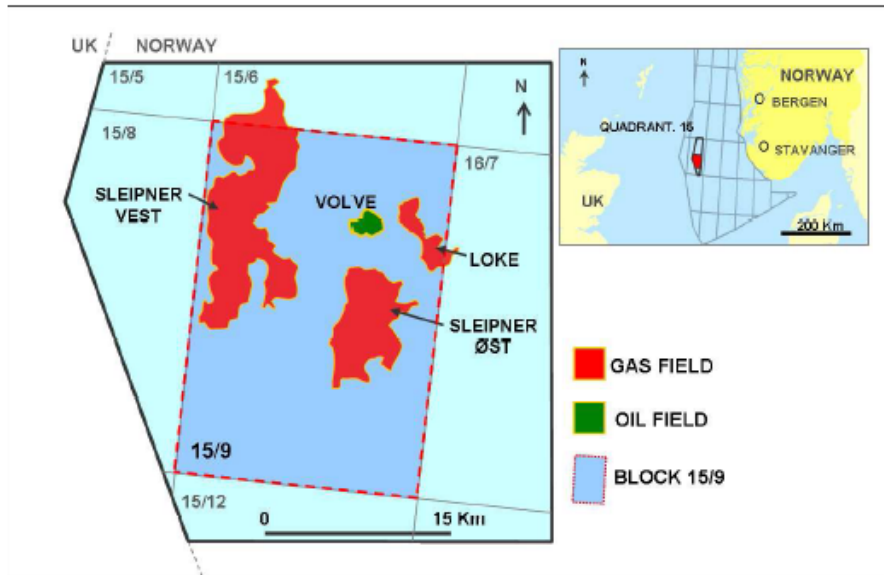
APPLICATION TO FIELD DATA

Volve Field is a Middle Jurassic oil reservoir located in the southern part of the Viking Graben in the gas/condensate-rich Sleipner area of the North Sea (Figure 5.1(a)). It is a small dome-shaped structure formed by the collapse of adjacent salt ridges during the Jurassic (Szydlik *et al.*, 2007). The reservoir is in the Middle Jurassic Hugin Sandstone Formation and the deposition was controlled by salt tectonics (Figure 5.1(b)).

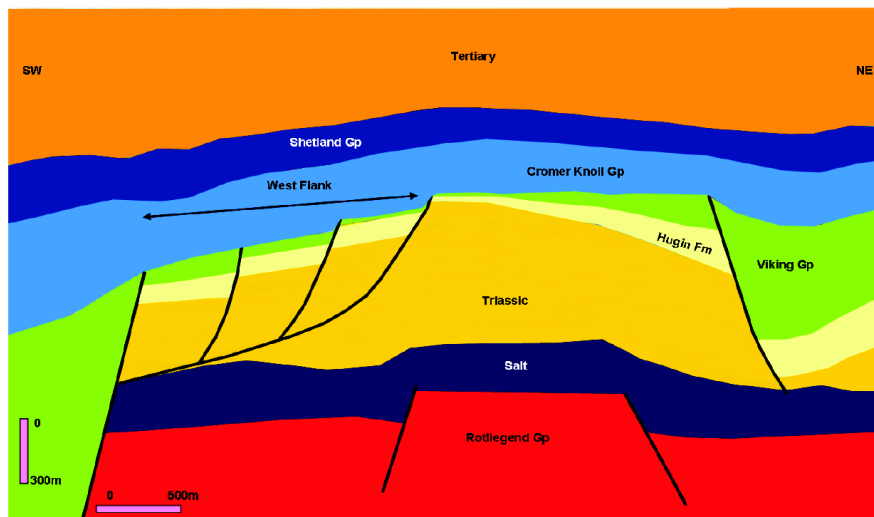
An ocean-bottom seismic (OBS) survey was acquired in 2002 over a $12.3 \text{ km} \times 6.8 \text{ km}$ area of the field (Figure 5.2). It is comprised of six swaths of four-component (4C) data and each swath includes two 6 km-long cables placed on the seafloor. The cables have 400 m spacing and move up 800 m after each swath. There are 240 receivers with an interval of 25 m on each cable. Dual source flip-flop shooting gave a 25 m shot separation and 100 m separation between sail lines.

The PP and PS OBS data were preprocessed using a standard sequence including wavelet shaping, noise and multiple attenuation techniques (Szydlik *et al.*, 2007). The VTI model produced by Statoil for prestack depth imaging is built using a layer-stripping approach. Each layer is updated by applying layer-based tomography and fitting check-shot data (Szydlik *et al.*, 2007). Flattening common-image gathers and minimizing misties between seismic and well data are repeated until the model is optimized. However, complete information about the VTI model-building process employed by Statoil is unavailable.

To test the joint MVA method introduced in the thesis, I use a 2D section from the 3D PP- and PS-wave data recorded by the cable laid along $y=2.8 \text{ km}$ (Figure 5.2). Two adjacent source lines ($y=2.8 \pm 0.025 \text{ km}$) include 481 shots with a shot interval



(a)



(b)

Figure 5.1: (a) Location of Volve field in the North Sea (figure courtesy of Statoil) and (b) a representative geologic cross-section of Volve field (after Akalin *et al.*, 2010).

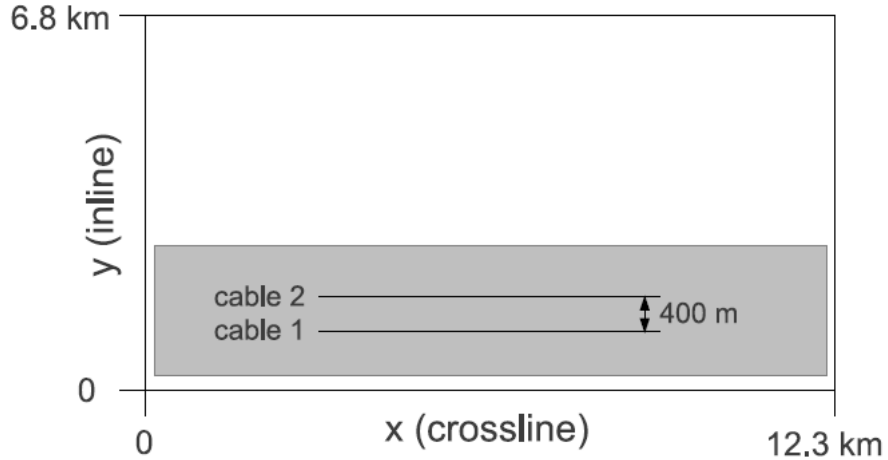
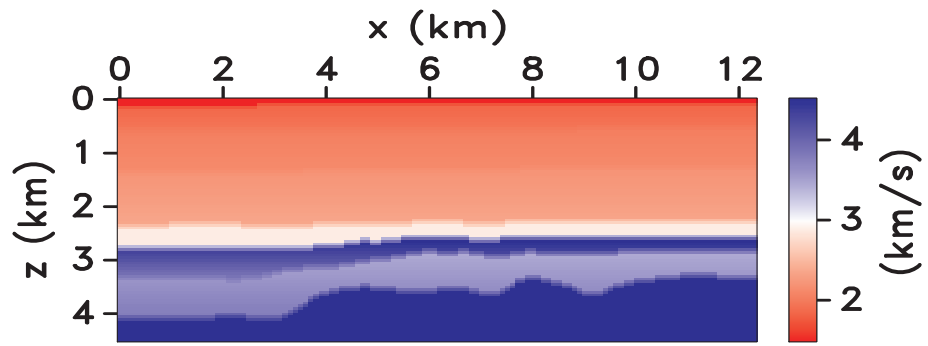


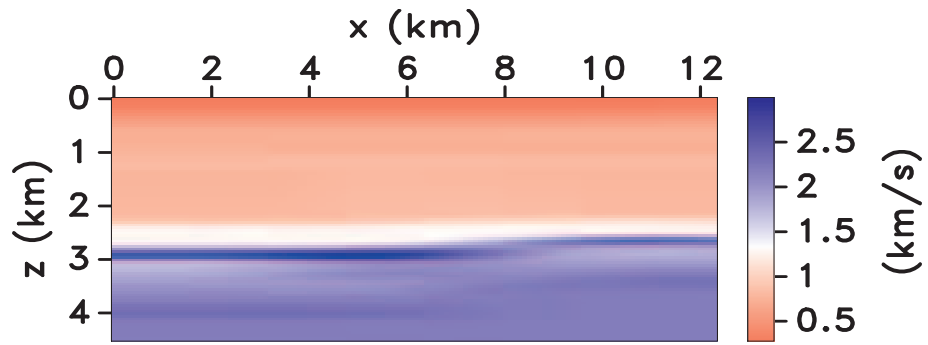
Figure 5.2: Geometry of the Volve 3D OBS survey. A pair of cables (black lines) was put on the seafloor with 400 m separation, and shots were acquired in a 12 km \times 2.4 km rectangular area (gray). There was an 800 m moveup between swaths (after Wang, 2012).

of 25 m.

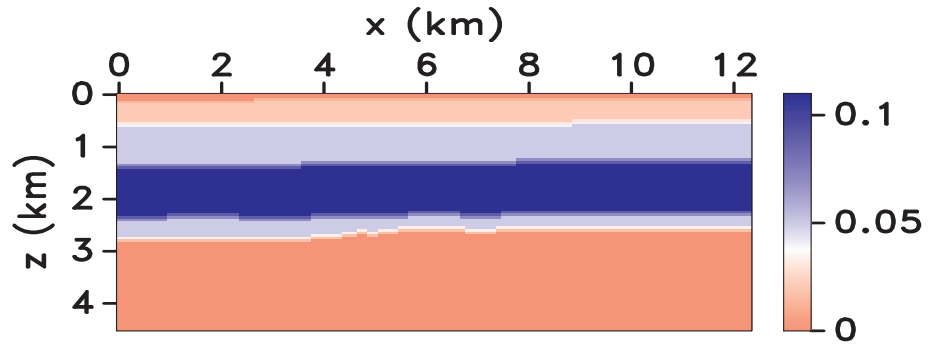
The joint MVA of PP- and PS-waves described above is applied to the CIGs from $x=3$ km to 9 km with an interval of 100 m. The initial model for the parameters V_{P0} , ϵ , and δ is taken from Wang (2012), who divided the section into eight layers based on key geologic horizons. The interval velocity V_{P0} in each layer is computed from the check-shot traveltimes recorded in two wells near the chosen line. The interval NMO velocity (V_{nmo}) and parameter η in each layer are estimated using nonhyperbolic moveout inversion (Tsvankin, 2005) applied to a CMP gather near one of the wells. The parameters V_{nmo} and η yield initial guesses for ϵ and δ at the well location. Then Wang (2012) obtained the initial VTI model by extrapolating the 1D profiles of V_{P0} , ϵ , and δ along the picked interfaces (Figure 5.3). Since check-shot data for shear waves were not available, a smoothed version of the shear-wave vertical-velocity model provided by Statoil is used here as the initial V_{S0} -field. The parameters V_{P0} , V_{S0} , ϵ , and δ are defined on a 100 m \times 50 m grid (Figure 5.3).



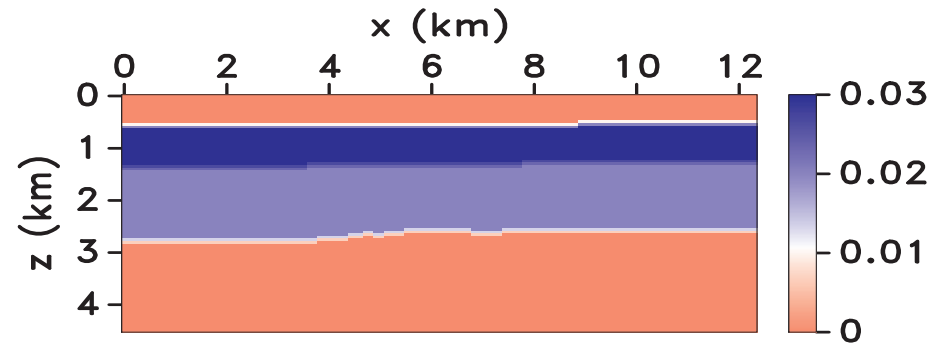
(a)



(b)



(c)



(d)

Figure 5.3: Initial VTI model for line $y=2.8$ km. The vertical velocities (a) V_{P0} and (b) V_{S0} and the anisotropy parameters (c) ϵ and (d) δ .

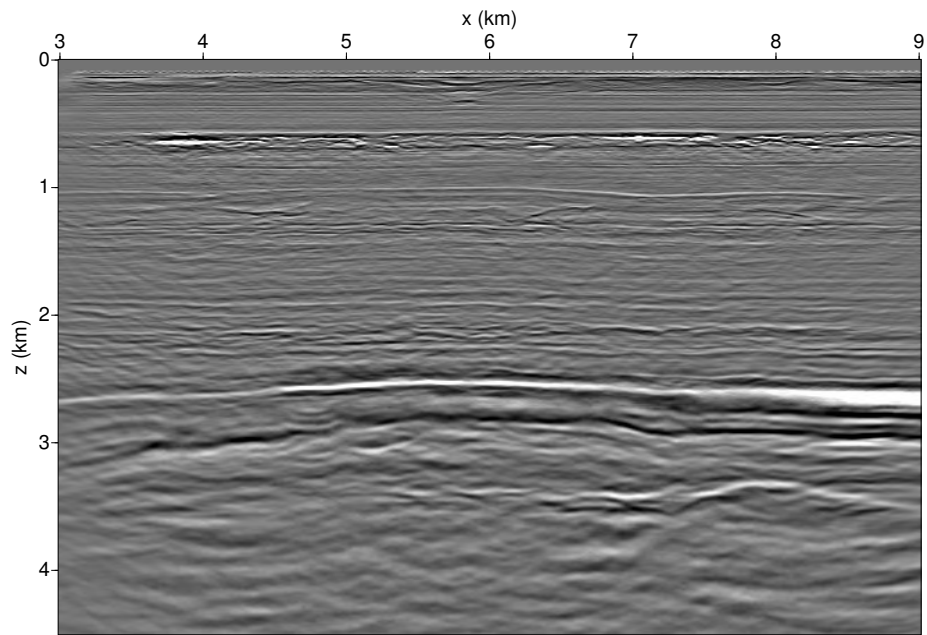
The PP and PS images migrated with the initial model are shown in Figure 5.4. There is a clearly visible mistie between the PP and PS sections for a reflector at a depth close to 2.5 km (top of the Cretaceous Unit); the depth of that reflector is smaller on the PS image.

To apply the PP+PS=SS method, I registered (correlated) five events on the PP and PS stacked sections. For each of these five events shear data were constructed by convolving the computed SS traveltimes with a Ricker wavelet. The codepthing term in the objective function includes the depths of these five reflectors on the PP and SS sections. The SS image generated with the initial model is shown in Figure 5.5. As expected, the CIGs of PP- and SS-waves obtained with the initial model parameters exhibit substantial residual moveout.

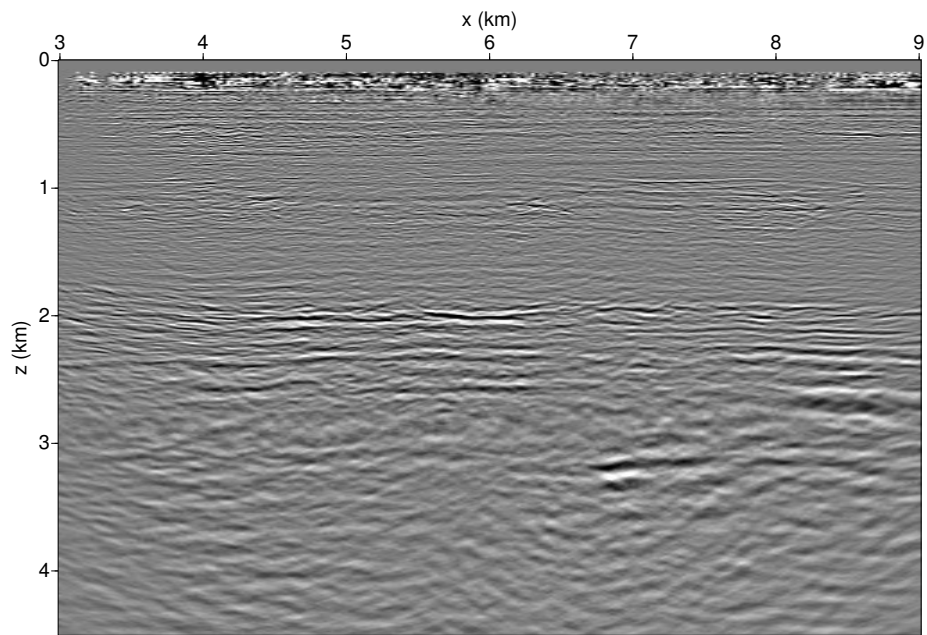
Because of the limited offset-to-depth ratio (smaller than 1.2 for $z > 3$ km), the accuracy of the effective parameters η and ϵ estimated from nonhyperbolic moveout (i.e., long-spread CIGs) decreases with depth. Therefore, the deeper layers are kept isotropic during model updating. The VTI model obtained after eight iterations of joint MVA of PP- and PS-waves (Figure 5.6) yields relatively flat PP and SS CIGs and depth-consistent PP and SS images (Figure 5.7).

The PS-wave depth image generated using PSDM with the estimated VTI model parameters is displayed in Figure 5.8. Compared with the section obtained using the initial model (Figure 5.4b), reflectors on the final image are better focused at depths around 3 km (Cretaceous unit). However, the image quality below the Base Cretaceous unconformity is still lower than that for PP-waves (Figure 5.7a). This is probably because the deeper layers (below 3 km) are kept isotropic during joint MVA, and PS-waves are more sensitive to anisotropy than PP-waves.

The estimated P-wave velocity field is close to horizontally layered, with the exception of a gently dipping interface at a depth of 3 km (Wang, 2012). Note that lateral parameter variations are suppressed by Wang's (2012) structure-guided op-



(a)



(b)

Figure 5.4: (a) PP- and (b) PS-wave images generated by Kirchhoff prestack depth migration with the initial model.

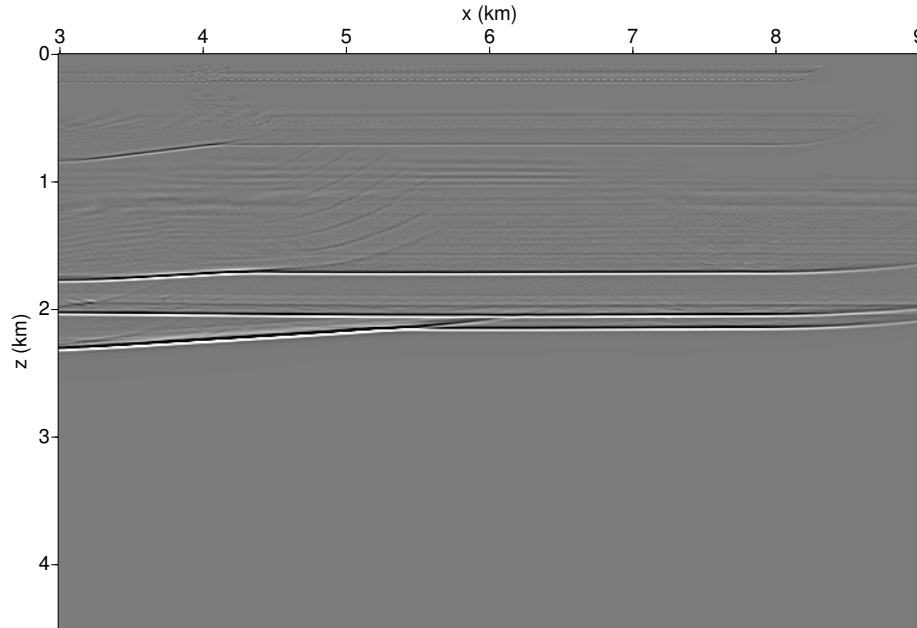
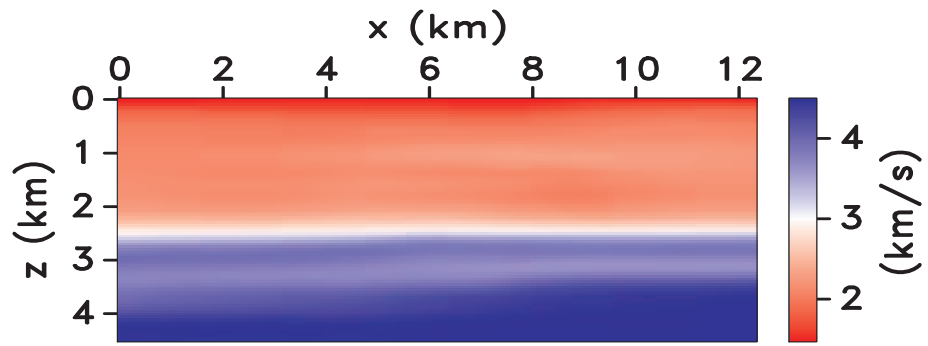


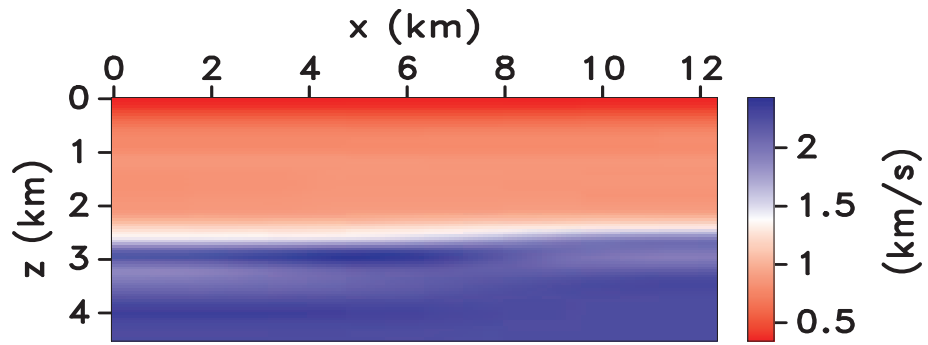
Figure 5.5: Image of the constructed SS-waves generated with the initial model.

erators and the Laplacian operator in my joint MVA of PP- and PS-waves. Note, however, that the Laplacian operator smooths the parameter field equally in the horizontal and vertical directions, while “structure-guided” regularization allows for more pronounced variations in the direction orthogonal to interfaces.

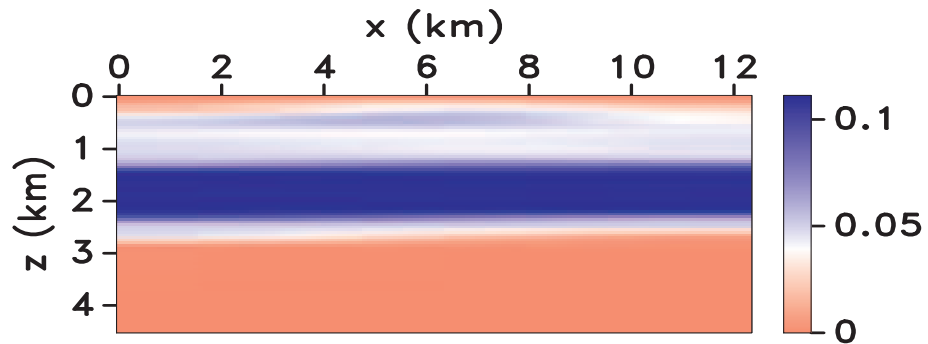
The final PP image (Figure 5.7a) produced with the help of the joint MVA of PP- and PS-waves does not differ much from that obtained by Wang (2012) using P-wave tomography. However, the reflectors in the Cretaceous unit look somewhat less coherent than those generated by Wang (2012). One possible reason is that Wang (2012) used a larger number of reflectors in building the velocity model. Also, although the dips are gentle, the TTI model employed by Wang (2012) is more geologically plausible and may yield more accurate anisotropy parameters than the VTI model used here. It is likely that better PP and PS depth images can be obtained with a TTI model, but the current version of the algorithm does not allow for a tilt of



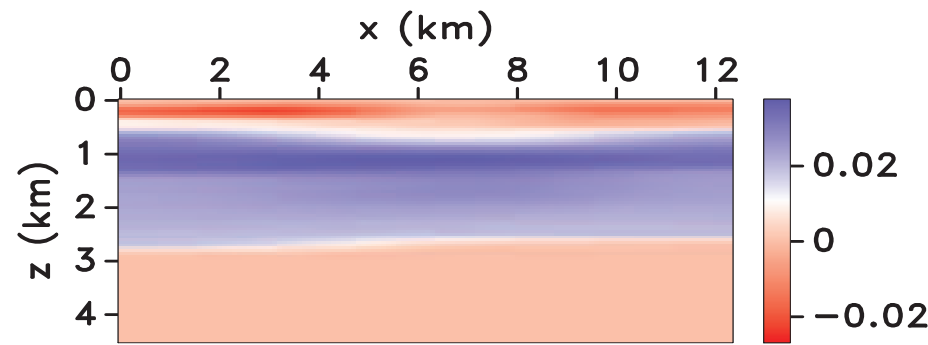
(a)



(b)

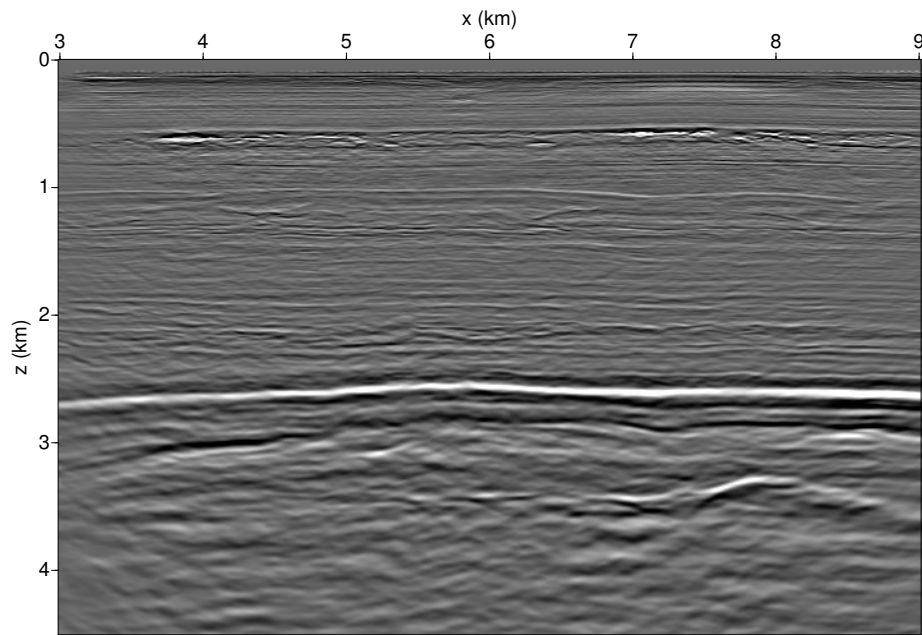


(c)

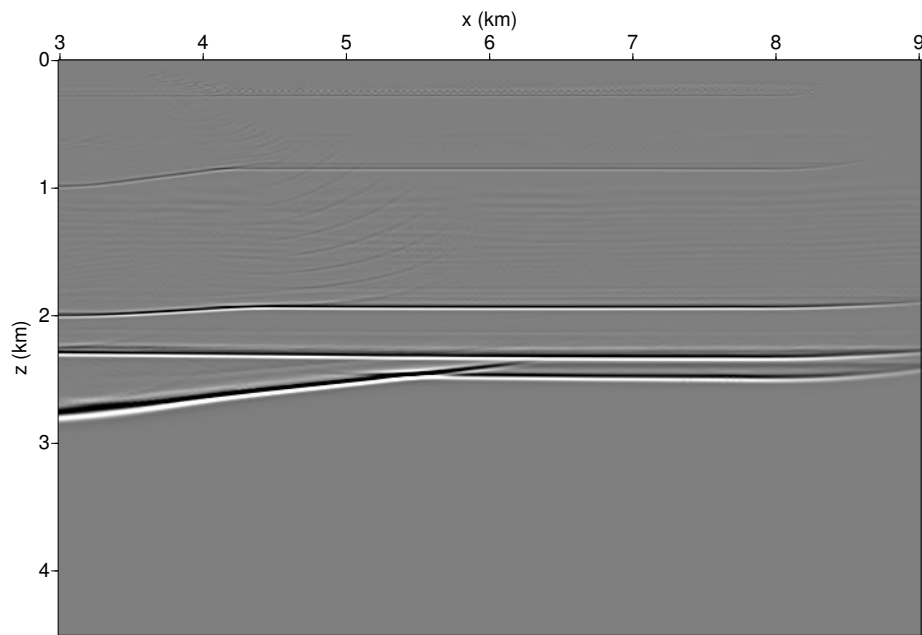


(d)

Figure 5.6: Estimated VTI model for line $y=2.8$ km from the Volve survey. The vertical velocities (a) V_{P0} and (b) V_{S0} and the anisotropy parameters (c) ϵ and (d) δ .



(a)



(b)

Figure 5.7: (a) PP- and (b) SS-wave depth images generated with the estimated model from Figure 5.6.

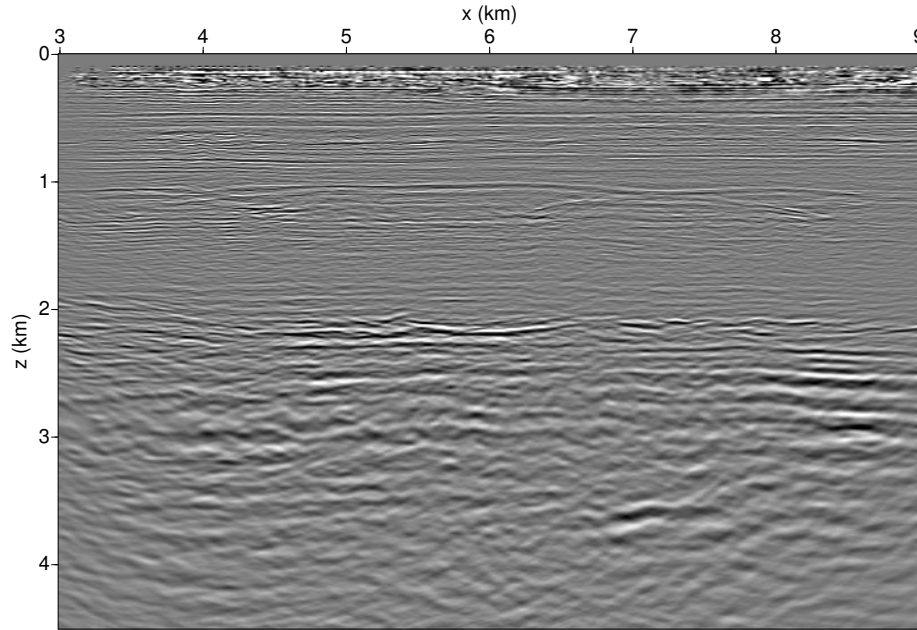


Figure 5.8: PS-wave depth image generated with the estimated model.

the symmetry axis as mentioned above. It is possible to tie the PP depth image with the PS depth image down to Base Cretaceous unconformity (the deepest event used to generate SS data). These depth-consistent PP and PS images provide a robust estimate of the V_{P0}/V_{S0} ratio, which can be used for reservoir characterization.

The final PP- and PS-wave images in Figures 5.7a and 5.8 are similar to those obtained with the VTI model provided by Statoil. It should be mentioned that Statoil's model has a higher spatial resolution than our model in Figure 5.6 because our updating procedure operated only with reflection data.

CHAPTER 6

CONCLUSIONS AND RECOMMENDATIONS

In the presence of moderate dips, combining PP reflection traveltimes with converted PS data may help reconstruct VTI velocity models in depth. The thesis presented an efficient algorithm for joint migration velocity analysis of PP- and PS-waves from heterogeneous VTI media.

To avoid problems caused by the moveout asymmetry and other undesirable inherent features of mode conversions, I first construct pure SS reflections using the PP+PS=SS method. After performing prestack Kirchhoff depth migration of PP and SS data, a nonhyperbolic semblance scan is used to evaluate the long-spread PP-wave residual moveout in common-image gathers. Then migration velocity analysis is performed jointly for PP- and SS-waves, which allows us to employ existing tomographic techniques devised for pure modes. The velocity model is updated iteratively by simultaneously minimizing the residual moveout in PP- and SS-wave gathers and misties between the migrated PP and SS sections.

Synthetic testing for VTI media composed of homogeneous layers confirmed that if both horizontal and moderately dipping PP and PS events are available, the joint MVA of 2D data may converge toward the correct depth model. The inversion becomes generally nonunique in the presence of laterally heterogeneous horizons. However, the parameters of factorized VTI layers (i.e., the parameters ϵ and δ in each layer are constant) with linear velocity variation can be resolved by correctly assuming that the velocities V_{P0} and V_{S0} vary linearly in space, and ϵ and δ in each layer are spatially invariant. The algorithm produces an acceptable approximation for the velocity field even if V_{P0} and V_{S0} are updated at each grid point, but the resulting image is not as well focused as the one obtained with linear $V_{P0}(x, z)$ and $V_{S0}(x, z)$

functions. Synthetic examples show that velocity estimation on a grid benefits from assigning larger weights to CIG flattening during several initial iterations. At later stages of the inversion, however, the convergence is improved by emphasizing the terms of the objective function responsible for codepthing and regularization.

The method was also applied to PP and PS(PSV) data recorded on a 2D line from a 3D OBS survey acquired at Volve field in the North Sea. A VTI model obtained by joint tomography of the recorded PP-waves and constructed SS-waves produced well-focused PP and PS depth images. The depth consistency between the PP and PS sections also indicates that the obtained anisotropic model and the ratio of the vertical P- and S-wave velocities are sufficiently accurate.

Therefore, PS-waves can play an important role in velocity model building for prestack depth migration of both PP and PS data. Multicomponent data also provide estimates of the shear-wave vertical velocity V_{S0} , which can be used in lithology prediction and reservoir characterization.

6.1 Recommendations for future work

Migration of 2D data implemented here assumes that the recorded reflected rays propagate in the vertical incidence plane. In the presence of out-of-plane events, 2D prestack depth migration may not be able to properly position some reflectors either in both PP- and PS-wave images. Extension of the 2D joint tomographic inversion to 3D is relatively straightforward, but it requires an efficient depth migration program to generate PP- and SS-wave CIGs. Parallel computing will likely be needed for tomographic inversion using a selection of reflectors in PP and SS images.

Event registration on PP and PS data volumes is an essential preprocessing step for the joint MVA. Developing a highly efficient automatic picker should help generate higher-quality SS data, which can improve the estimated anisotropic model.

The Laplacian operator used here to constrain model updates smooths the parameter fields equally along the horizontal and vertical directions and does not preserve

the interfaces. A better option is the “structure-guided” smoothing operator, which penalizes parameter variations along the interfaces.

The algorithm developed here is designed for heterogeneous VTI media. In complex geologic settings including dipping shale layers, a more appropriate and plausible model is TTI. The tilt of the symmetry axis typically varies laterally and can cause serious migration errors when the image is obtained with a VTI model. The influence of tilt, however, generally creates uncertainty in migration velocity analysis. Generalization of the proposed methodology to heterogeneous TTI media is an important direction for future research.

REFERENCES CITED

- Adler, F., Baina, R., Soudani, M. A., Cardon, P., & Richard, J. 2008. Nonlinear 3D tomographic least-squares inversion of residual moveout in Kirchhoff prestack-depth-migration common-image gathers. *Geophysics*, **73**(5), VE13–VE23.
- Akalin, A., Thompson, M., Mispel, J., & Rundhovde, E. 2010. Volve - How close communication between the asset team and research was an enabler for field development. *Petex Expanded Abstracts*.
- Alkhalifah, T., & Tsvankin, I. 1995. Velocity analysis for transversely isotropic media. *Geophysics*, **60**, 1550–1566.
- Audebert, F., Granger, P. Y., & Herrenschmidt, A. 1999. CCP-scan technique (1): True common conversion point sorting and converted wave velocity analysis solved by PP and PS Pre-Stack Depth Migration. *SEG Technical Program Expanded Abstracts*, **18**, 1186–1189.
- Bakulin, A., Woodward, M., Nichols, D., Osypov, K., & Zdraveva, O. 2010. Building tilted transversely isotropic depth models using localized anisotropic tomography with well information. *Geophysics*, **75**(4), D27–D36.
- Broto, K., Ehinger, A., Kommedal, J. H., & Folstad, P. G. 2003. Anisotropic travelttime tomography for depth consistent imaging of PP and PS data. *The Leading Edge*, 114–119.
- Donati, M., & Stewart, R. 1998. Migration velocity analysis by perturbation for converted waves. *CREWES Research Report*, **10**, 28–36.
- Du, Q., Li, F., Ba, J., Zhu, Y., & Hou, B. 2012. Multicomponent joint migration velocity analysis in the angle domain for PP-waves and PS-waves. *Geophysics*, **77**(1), U1–U13.
- Foss, S.-K., Ursin, B., & de Hoop, M. V. 2005. Depth-consistent reflection tomography using PP and PS seismic data. *Geophysics*, **70**(5), U51–U65.
- Gajewski, D., & Pšenčík, I. 1987. Computation of high-frequency seismic wavefields in 3-D laterally inhomogeneous anisotropic media. *Geophysical Journal of the Royal Astronomical Society*, **91**(2), 383–411.

- Grechka, V., & Dewangan, P. 2003. Generation and processing of pseudo-shear-wave data: Theory and case study. *Geophysics*, **68**(6), 1807–1816.
- Grechka, V., & Tsvankin, I. 2002a. The joint nonhyperbolic moveout inversion of PP and PS data in VTI media. *Geophysics*, **67**, 1929–1932.
- Grechka, V., & Tsvankin, I. 2002b. PP+PS=SS. *Geophysics*, **67**(6), 1961–1971.
- Grechka, V., Tsvankin, I., Bakulin, A., Hansen, J. O., & Signer, C. 2002a. Joint inversion of PP and PS reflection data for VTI media: A North Sea case study. *Geophysics*, **67**(5), 1382–1395.
- Grechka, V., Pech, A., & Tsvankin, I. 2002b. Multicomponent stacking-velocity tomography for transversely isotropic media. *Geophysics*, **67**(5), 1564–1574.
- Liu, Z. 1997. An analytical approach to migration velocity analysis. *Geophysics*, **62**(4), 1238–1249.
- Sarkar, D., & Tsvankin, I. 2004. Migration velocity analysis in factorized VTI media. *Geophysics*, **69**, 708–718.
- Stopin, A., & Ehinger, A. 2001. Joint PP PS tomographic inversion of the Mahogany 2D 4-C OBC seismic data. *SEG Technical Program Expanded Abstracts*, **20**(1), 837–840.
- Stork, C. 1992. Reflection tomography in the postmigrated domain. *Geophysics*, **57**, 680–692.
- Szydlík, T., Smith, P., Way, S., Aamodt, L., & Friedrich, C. 2007. 3D PP/PS prestack depth migration on the Volve field. *First Break*, **25**, 43–47.
- Thomsen, L. 1986. Weak elastic anisotropy. *Geophysics*, **51**(10), 1954–1966.
- Thomsen, L. 1999. Converted-wave reflection seismology over inhomogeneous, anisotropic media. *Geophysics*, **64**, 678–690.
- Tsvankin, I. 2005. *Seismic signatures and analysis of reflection data in anisotropic media*. 2nd edn. Elsevier Science Publishing Company, Inc.
- Tsvankin, I., & Grechka, V. 2000. Dip moveout of converted waves and parameter estimation in transversely isotropic media. *Geophysical Prospecting*, **48**, 257–292.
- Tsvankin, I., & Grechka, V. 2011. *Seismology of azimuthally anisotropic media and seismic fracture characterization*. Society of Exploration Geophysicists.

- Tsvankin, I., & Thomsen, L. 1995. Inversion of reflection traveltimes for transverse isotropy. *Geophysics*, **60**, 1095–1107.
- Wang, B., Pann, K., & Meek, R. A. 1995. Macro velocity model estimation through model based globally-optimized residual-curvature analysis. *SEG Technical Program Expanded Abstracts*, **14**(1), 1084–1087.
- Wang, X. 2012. *Anisotropic velocity analysis of P-wave reflection and borehole data*. Ph.D. thesis, Colorado School of Mines.
- Wang, X., & Tsvankin, I. 2012. Ray-based gridded tomography for tilted transversely isotropic media. *Geophysics*, in print.
- Zhou, C., Jiao, J., Lin, S., Sherwood, J., & Brandsberg-Dahl, S. 2011. Multiparameter joint tomography for TTI model building. *Geophysics*, **76**(5), WB183–WB190.

APPENDIX - PARAMETER-UPDATING METHODOLOGY

I extend the MVA algorithm of Wang & Tsvankin (2012) to the combination of PP and SS data, where the SS-waves are constructed by the PP+PS=SS method. In addition to flattening PP and SS image gathers, I also perform codepthing to ensure that the reflectors on the PP and SS sections are imaged at the same depth. Following Wang & Tsvankin (2012), the variance Var of the migrated depths can be written as

$$Var = \sum_{j=1}^U \sum_{k=1}^M [z(x_j, h_k) - \hat{z}(x_j)]^2, \quad (\text{A.1})$$

where U is the number of image gathers used in the velocity update, M is the number of offsets in image gathers, x_j is the midpoint, h_k is the half-offset, and $\hat{z}(x_j) = (1/M) \sum_{k=1}^M z(x_j, h_k)$ is the average migrated depth at x_j . By minimizing the variances Var_P (for P-waves) and Var_S (for S-waves), one can flatten CIGs for both modes. The difference between the migrated depths of PP- and SS-waves from the same reflector can be estimated as:

$$Var_{P-S} = \sum_{j=1}^U [\hat{z}_P(x_j) - \hat{z}_S(x_j)]^2. \quad (\text{A.2})$$

Minimizing Var_{P-S} makes it possible to tie the PP and SS sections in depth. Differentiating the variances with respect to the parameter updates $\Delta\lambda$ and setting $\partial V/\partial(\Delta\lambda) = 0$ yields

$$\mathbf{A}_P^T \mathbf{A}_P \Delta\lambda = -\mathbf{A}_P^T \mathbf{b}_P \quad (\text{A.3})$$

$$\mathbf{A}_S^T \mathbf{A}_S \Delta\lambda = -\mathbf{A}_S^T \mathbf{b}_S \quad (\text{A.4})$$

$$\mathbf{D}^T \mathbf{D} \Delta\lambda = -\mathbf{D}^T \mathbf{y}, \quad (\text{A.5})$$

where \mathbf{A} is a $M * U$ by $W * N$ matrix with elements $g_{jk,ic} - \hat{g}_{j,ic}$, where $g_{jk,ic} = \partial z(x_j, h_k)/\partial \lambda_{ic}$ and $\hat{g}_{j,ic} = (1/M) \sum_{k=1}^M g_{jk,ic}$. The subscripts P and S denote P- and S-waves, respectively. The vector \mathbf{b} contains $M * U$ elements defined as $z(x_j, h_k) - \hat{z}(x_j)$.

\mathbf{D} is also a $M * U$ by $W * N$ matrix and its elements are $g_{jk,ic}^P - g_{jk,ic}^S$, where $g_{jk,ic}^P$ is computed for P-waves and $g_{jk,ic}^S$ for S-waves. The $M * U$ vector \mathbf{y} has elements $z^P(x_j, h_k) - z^S(x_j, h_k)$. As discussed in Wang & Tsvankin (2012), the derivatives $g_{jk,ic}$ are found by differentiating phase velocity with respect to the medium parameters along the raypath.